Y3.N88:25/2520
COMPLETED
97

NUREG/CR-2520

ORIGINAL

A Hydrodynamic Analysis of the Electron Beam Vaporization Experiments for UO_2

Prepared by B. D. Ganapol, B. A. Clark, M. S. Smith, G. W. Sowers

Department of Nuclear and Energy Engineering
The University of Arizona

Prepared for
U.S. Nuclear Regulatory
Commission

NOTICE

This report was prepared as an account of work sponsored by an agency of the United States Government. Neither the United States Government nor any agency thereof, or any of their employees, makes any warranty, expressed or implied, or assumes any legal liability of responsibility for any third party's use, or the results of such use, of any information, apparatus, product or process disclosed in this report, or represents that its use by such third party would not infringe privately owned rights.

Availability of Reference Materials Cited in NRC Publications

Most documents cited in NRC publications will be available from one of the following sources:

1. The NRC Public Document Room, 1717 H Street, N.W.
   Washington, DC 20555
2. The NRC/GPO Sales Program, U.S. Nuclear Regulatory Commission,
   Washington, DC 20555
3. The National Technical Information Service, Springfield, VA 22161

Although the listing that follows represents the majority of documents cited in NRC publications, it is not intended to be exhaustive.

Referenced documents available for inspection and copying for a fee from the NRC Public Document Room include NRC correspondence and internal NRC memoranda; NRC Office of Inspection and Enforcement bulletins, circulars, information notices, inspection and investigation notices; Licensee Event Reports, vendor reports and correspondence; Commission papers; and applicant and licensee documents and correspondence.

The following documents in the NUREG series are available for purchase from the NRC/GPO Sales Program: formal NRC staff and contractor reports, NRC-sponsored conference proceedings, and NRC booklets and brochures. Also available are Regulatory Guides, NRC regulations in the *Code of Federal Regulations*, and *Nuclear Regulatory Commission Issuances*.

Documents available from the National Technical Information Service include NUREG series reports and technical reports prepared by other federal agencies and reports prepared by the Atomic Energy Commission, forerunner agency to the Nuclear Regulatory Commission.

Documents available from public and special technical libraries include all open literature items, such as books, journal and periodical articles, and transactions. *Federal Register* notices, federal and state legislation, and congressional reports can usually be obtained from these libraries.

Documents such as theses, dissertations, foreign reports and translations, and non-NRC conference proceedings are available for purchase from the organization sponsoring the publication cited.

Single copies of NRC draft reports are available free upon written request to the Division of Technical Information and Document Control, U.S. Nuclear Regulatory Commission, Washington, DC 20555.

Copies of industry codes and standards used in a substantive manner in the NRC regulatory process are maintained at the NRC Library, 7920 Norfolk Avenue, Bethesda, Maryland, and are available there for reference use by the public. Codes and standards are usually copyrighted and may be purchased from the originating organization or, if they are American National Standards, from the American National Standards Institute, 1430 Broadway, New York, NY 10018.

GPO Printed copy price $5.00

BEST DOCUMENT AVAILABLE

NUREG/CR-2520
R7

A Hydrodynamic Analysis of the Electron Beam Vaporization Experiments for UO_2

Manuscript Completed: June 1982
Date Published: July 1982

Prepared by
B. D. Ganapol, B. A. Clark, M. S. Smith, G. W. Sowers

Department of Nuclear and Energy Engineering
The University of Arizona
Tucson, AZ 85721

Prepared for
Division of Accident Evaluation
Office of Nuclear Regulatory Research
U.S. Nuclear Regulatory Commission
Washington, D.C. 20555
NRC FIN A4065

I

BLANK PAGE

ABSTRACT

The electron-beam experiments designed to generate high temperature vapor pressure data for UO_2 vapor is analyzed by three hydrodynamic codes SIMMER, FARA and VIOLET. The physical and numerical modeling in each code is different thus providing a modeling error associated with the analysis. Agreement with the experiment is rather poor indicating that the rate dependent specific heat capacity model proposed by Benson may not be a physical reality.

BLANK PAGE

TABLE OF CONTENTS

	Page
ABSTRACT	iii
LIST OF TABLES	vii
LIST OF ILLUSTRATIONS	viii
1. INTRODUCTION	1
2. DESCRIPTION OF SANDIA E-BEAM EXPERIMENTS	2
2.1 Experimental Geometry	2
2.2 Energy Deposition	3
2.3 Experimental Results	3
2.4 Comparisons with Existing Data	3
3. COMPUTER CODES	4
3.1 SIMMER-II	4
3.1.1 SIMMER-II Code Description	4
3.1.2 Geometrical Model	5
3.1.3 Graphite Motion Model	5
3.1.4 Global Momentum Model	6
3.1.5 Energy Deposition	6
3.2 The FARA Code	6
3.2.1 Code Description	6
3.2.2 Numerical Solution	7
3.2.3 Benchmark Problems	11
3.3 The VIOLET Code	14
3.3.1 Code Description	14
3.3.2 Analytical Benchmark	15
3.4 Inter-code Comparison	15
4. RESULTS AND DISCUSSION	15
4.1 SIMMER-II Analysis	15
4.1.1 Initial Acceleration	16
4.1.2 Intermediate Motion	17
4.1.3 Long Time Motion	17

Page

4.1.4 Variation of EOS. 17
4.1.5 Sensitivity to the Initial UO_2 Density. 17

4.2 FARA Analysis. 18
4.3 VIOLET Analysis. 18

5. DISCUSSION OF RESULTS 18

5.1 Possible Additional Pressure Sources 19
5.2 Modeling Uncertainties 19
5.3 Summary. 20

6. REFERENCES. 55

LIST OF TABLES

Table		Page
1	Sample of Thicknesses.	21
2	Features of Codes.	21
3	Estimated Maximum Velocities from Thermal Expansion.	22
4	Piston Velocities.	22
5	Admissible Contents in LMFBR Fuel Impurities which can Give Rise to Pressure Contributions in an EOS-Experiment	23
6	Non-Fuel Vapor Gas Release	23

LIST OF ILLUSTRATIONS

Figure		Page
1	Experiment Schematic.	24
2	Spatial Variation of the Energy Deposition.	25
3	Piston Displacement Variation with Energy Deposition.	26
4	Piston Velocity Variation with Energy Deposition.	27
5	Solid UO_2 Heat Capacity	28
6	EOS in Pressure-Energy Format	29
7	Comparison of e-beam Results with Other Data.	30
8	Normalized Source Variation in Time.	31
9	Energy Input Benchmark.	32
10	Frictional Flow Benchmark	33
11	Heat Transfer Benchmark	34
12	Shock Tube Benchmark.	35
13	Rarefaction Benchmark	36
14a	Adiabatic Blowoff Benchmark	37
14b	Adiabatic Blowoff Benchmark	38
14c	Adiabatic Blowoff Benchmark	39
15	Position of Peak Density for Temperature Spike.	40
16	Spreading of Density Pulse in SIMMER Calculation.	41
17	SIMMER-II Velocity Results for 2030 J/g Energy Deposition . .	42
18	Spatial Liquid Velocity Variation	43
19	Spatial Variation of the Pressure	44

List of Illustrations--Continued

Figure		Page
20	Experimental Data Points for Several Cases.	45
21	Comparison of Experimental Fit to Numerical Results for the 1860 J/g Energy Pulse	46
22	Comparison of Experimental Fit to Numerical Results for the 1990 J/g Energy Pulse	47
23	Comparison of Experimental Fit to Numerical Results for the 2030 J/g Energy Pulse	48
24	Piston Velocity for 2030 J/g Energy Deposition with Benson EOS.	49
25	Pressure on Piston Pace for 2030 J/g Energy Deposition with Benson EOS	50
26	Piston Velocity for 2030 J/g Energy Deposition with Menzes EOS.	51
27	Velocity Profile for 2030 J/g Energy Deposition with Benson EOS	52
28	Comparison of the Piston Velocity for 2030 J/g Deposition . .	53
29	Pressure Contribution from Fuel Impurity Gases Compared to that of Pure Fuel	54

1. INTRODUCTION

Core disassembly analysis has traditionally been and will continue to be a major consideration in fast reactor safety investigations. From the examination of a postulated mechanical core disassembly and subsequent core expansion, the potential for radioactive release resulting from damage to the primary LMFBR containment can be estimated. Typically, the disassembly description consists of three fundamental models: hydrodynamic core motion, neutronic interaction and core thermodynamic behavior. In this report, we are concerned with the thermodynamic modeling of an LMFBR core undergoing disruption due to a postulated core disruptive accident (CDA). The thermodynamic modeling is effected through an equation of state (EOS) of the core material which specifies the pressure-density-temperature or internal energy evolution of the core components. To properly describe this evolution, an adequate data base is required for incorporation into the EOS model. To this end, in the United States, Federal Republic of Germany, France and the United Kingdom, a considerable effort has been directed toward the experimental determination of the fuel vapor pressure at temperatures characteristic of LMFBR disassembly and expansion events. Currently, the high temperature (up to 6000°K) UO_2 EOS data base consists of

(a) extrapolations of low temperature data [1]
(b) laser surface heating experiments [2-3]
(c) volume joule heating experiments [4]
(d) volume nuclear heating experiments [5]
(e) electron-beam (e-beam) heating experiments [6].

At Sandia National Laboratory, under the sponsorship of the Nuclear Regulatory Commission, volume heating of unirradiated urania (UO_2) samples have been performed. To date, this program has included electron-beam (e-beam) and nuclear heating experiments in an attempt to provide vapor pressure data for UO_2 to temperatures of about 5000°K.

The results of the e-beam experiments have been most conveniently obtained in a pressure-energy format. Therefore, in order to compare the results from the e-beam experiments to existing EOS data, a specific heat capacity (C_p) model is required. It has been found that discrepancies of more than a factor of 2 exist between the extrapolated pressure-temperature data translated into a pressure-energy format (using the heat capacity data of Kerrish and Clifton [8] and Leibowitz [9]) and the e-beam experimental results. To explain the disagreement, a rather unconventional rate dependent C_p model has been proposed [6] based on the rapid heating in the e-beam experiments as compared to previous experiments. If true, a dynamic C_p model would, in general, generate an earlier accident termination due to fuel disassembly than that predicted by a static model and, consequently, less fission energy deposition. However, with the dynamic model, a significantly larger amount of fuel vapor would be generated at higher pressures and temperatures resulting in the potential for an increased amount of work-energy to be imparted to the sodium pool and reactor vessel head. Thus, the resolution of the discrepancies in the EOS

could be important in specifying the accident progression after core disassembly including post-accident heat removal and the potential for radiological release.

It will be the purpose of this work, therefore, to perform an experimental analysis of the e-beam experiments in order to better understand the thermodynamic behavior of urania under CDA conditions. The particular emphasis of our study will be on the hydrodynamic behavior of the fuel sample undergoing rapid energy deposition. Specifically, our approach will be to model the EOS experiments with three hydrodynamic computer codes, SIMMER-II, FARA, VIOLET, each with different models and numerical techniques. In this way, we hope to bracket the modeling as well as numerical error in the analysis. To establish confidence in the newly developed codes, FARA and VIOLET, analytical benchmark solutions for relatively idealistic and uncomplicated flow situations will be used to check the numerical schemes. The KACHINA hydrodynamic module in SIMMER-II [10] has been extensively tested [11] and therefore need not be benchmarked in this work. In addition, the codes will be tested on a common problem in order to establish inherent differences due to numerical solution algorithms and modeling. Finally, the three codes will be used to model and interpret the Sandia e-beam experiments. Using this comprehensive approach, we hope to provide a best estimate of the hydrodynamic behavior and an experimental interpretation of the Sandia e-beam experiments.

2. DESCRIPTION OF SANDIA E-BEAM EXPERIMENTS

The electron-beam heating experiments are extensively described by Benson [6]. In this section the geometry, energy deposition, and results of the experiment are discussed with the descriptions limited to points of interest in this analysis. Detailed information is available in the reference cited above.

2.1 Experimental Geometry

The experimental geometry is shown schematically in Figure 1 (note the drawing is not to scale). The powdered urania sample with nominal particle diameter of 2μ is situated between two graphite pistons, or plugs of diameter 6.35×10^{-3}m. The sample thicknesses in mass per unit area for the five experimental runs of different energy deposition are given in Table 1. The macroscopic UO_2 density is reported to be about 2×10^3 kg/m^3 with a 50-80% relative error [12].*

Following the energy deposition from the Relativistic Electron Beam Accelerator (REBA) facility, the graphite pistons will move under the influence of the forces generated within the sample. The piston displacement is recorded with a streak camera and the energy deposited within the sample is inferred from a calorimeter measurement and electron transport calculation. A calorimeter plate is located behind the outer piston and the specific energy deposited in the plate is measured with an optical pyrometer. By neglecting heat losses and the graphite piston compressibility, the sample vapor pressure can then be related to the second derivative of the piston displacement through Newton's second law.

*D.A. Bensen, private communication.

Combined with the specific energy measurement, the pressure-energy variation can thus be obtained by varying the energy deposition.

2.2 Energy Deposition

The energy source used to heat the urania sample is the REBA facility which supplies an electron beam of 1.2 MeV average electron energy. The accelerator operates in a pulsed mode with each pulse approximately Gaussian in time with 0.6 μs full width at half-maximum. The spatial variation of the energy deposition in the sample is determined from a static electron transport deposition profile [13]. It is assumed that the energy is deposited in a short time compared to the time for initiation of the sample motion, essentially allowing the energy deposition profile to be determined independently of the material motion. From the calorimeter plate specific energy measurement and the normalized energy distribution, one obtains the desired energy distribution in the sample (see Figure 2). The large graphite heat capacity keeps the graphite below its melting temperature (2000°C); and, therefore, the pistons are relatively unaffected by the energy deposition of the e-beam. In addition, due to the short duration of the experiment (2-20μs) and the relatively low thermal conductivity of the two phase urania mixture, the heat transfer from the sample to the graphite can be neglected.

2.3 Experimental Results

The graphite piston displacements and velocities for the five experiments, each with different total energy deposition, are given (versus time) in Figures 3 and 4 respectively. Two fundamental velocity variations in time can clearly be identified from physical considerations. Initially, solid thermal expansion and liquid urania impact produce a rapid piston acceleration; thereafter, a nearly isentropic vapor expansion dominates the piston motion. It should be noted for future reference that the vapor expansion velocity profiles for the data points given exhibits an oscillatory behavior indicitive of wave phenomena.

2.4 Comparisons with Existing Data

Traditionally EOS data has been expressed in a pressure-temperature format. Therefore, as mentioned earlier, to compare Benson's data in a pressure-energy format, a heat capacity model is required to translate energy into temperature or vice versa. Bergeron [7] has examined Frenkel defect formation in UO_2 and has concluded that, for low temperatures, defect transition times could be on the order of milliseconds. This analysis therefore lends credence to the Benson conjecture that due to the short duration of the experiment, the contribution from defect formation would not be present. On the other hand, recent theories [14,15] have indicated that the Frenkel defect formation could not possibly have produced the observed anomalous heat capacity near melting (see Figure 5) which is absent in Benson's theory. In particular, McInnes [15] believes the anomaly to be electronic in nature and therefore observable on a microsecond time scale. These contrasting theories tend to cloud the issue as to which heat capacity model is most

applicable to the e-beam experimental data. Therefore, to provide a comparison, two average solid heat capacities, with and without the anomalous contribution, will be used to translate the data into the proper format.

In Figure 6 a pressure-energy plot is given for the extrapolated Menzies EOS [1] (the most generally accepted EOS) with and without the anomalous contribution to the specific heat. Better agreement between the experimental and Menzies curves is obtained using the C_p without the anomalous contribution. In addition, a comparison can be made with experiments of the same time scale as shown in Figure 7. Also plotted is an extrapolation of low temperature data [18] using the heat capacity without (model 1) and with (model 2) the anomalous contribution to the heat capacity. Due to uncertainties in the thermal losses in the nuclear heating experiments, only bounds on the pressure can be reported for the data of reference 5. It is interesting to note that within the error of the respective experiments, the data seems to support Benson's claim of a rate-dependent specific heat capacity.

From theoretical and experimental considerations, therefore, we see that a rate dependent C_p is possible. In this work, we will attempt to provide a hydrodynamic verification of this concept with the following sections describing the modeling procedures.

3. COMPUTER CODES

In an attempt to understand the thermodynamic behavior of UO_2 during the e-beam experiments, an experimental analysis will be performed. The basic philosophy of the analysis will be to model the experiment with relatively simple "off the shelf" methods embodied in three distinct computer codes. The codes will contain different models as well as numerical methods. In this way, we hope to bracket the numerical as well as the modeling error. In the analysis, specific heats indicative of both the static and dynamic theories will be used. This section contains the descriptions of the three codes, SIMMER-II, FARA and VIOLET, which will serve as the fundamental tools of the analysis.

3.1 SIMMER-II

3.1.1 SIMMER-II Code Description

SIMMER-II is a comprehensive fast reactor accident analysis code developed at Los Alamos National Laboratory [10] for use in NRC confirmatory and licensing applications. In its most complete form, SIMMER-II includes a neutron transport or diffusion theory option which, of course, will not be needed for our analysis. The KACHINA Eulerian fluid flow code [10] is used to solve the hydrodynamics equations in a "semi-implicit" fashion. In general, three fields are considered; structure, liquid and vapor, with solid particles allowed in the liquid field. Each field may contain several components, including fissile fuel, fertile fuel, steel, sodium control material and fission gas, where the fuel components share the same EOS. In the analysis to follow only

fissile fuel, fertile fuel, steel and fission gas components will be used. The UO_2 powdered sample is modeled initially as solid fissile fuel particles in the liquid field and the graphite piston is modeled as solid steel with the equation of state appropriately modified to reflect graphite properties. The heat transfer models include convection and conduction heat transfer within a given cell with no heat transfer between cells.

3.1.2 Geometrical Model

From Figure 1, it is seen that the piston geometry is not symmetric. Benson [6], however, has reported that no gross motion of the center of the sample mass was observed; therefore, to a good approximation, the pistons can be considered to move independently requiring only one piston to be simulated. The sample is assumed symmetric about the center with half the sample occupying 10 mesh cells. Graphite is placed in the outermost cells with the graphite motion simulated by a moving graphite-UO_2 interface as described in the following section.

3.1.3 Graphite Motion Model

A graphite motion model was incorporated into the SIMMER-II program to allow limited movement of the structure field in order to simulate the piston motion. The graphite-UO_2 interface is assumed to move under the influence of the pressure gradient across the piston and the net rate of change of momentum imparted to the piston surface. The force resulting from the pressure gradient is simply

$$F_p = (P_{UO_2} - P_o)A \tag{3.1}$$

where P_{UO_2} is the pressure at the graphite surface and P_o is the ambient pressure. The force arising from momentum transfer is

$$F_c = M\ \Delta V/\Delta t \tag{3.2}$$

where M is the mass of the colliding fluid. The calculation of ΔV is dependent on the degree of elasticity of the fluid impact. A fully elastic collision will result in the liquid traveling at its previous velocity in the opposite direction after impact. An inelastic collision will result in zero velocity relative to the piston after the collision. A parameter e is introduced such that

$$\Delta V = e\ V \tag{3.3}$$

where V is relative to the piston and e can assume values from 1 (completely inelastic collision) to 2 (completely elastic collision). The acceleration of the piston is therefore due to the sum of the forces or

$$a = (P_{UO_2} - P_o)/\xi + eMV/\xi A\Delta t \tag{3.4}$$

where ξ is the mass per unit sample area. With Eq. (3.4), an updated acceleration is determined at the beginning of each time step. The latest acceleration and the acceleration during the previous time step are then linearly extrapolated to provide an average acceleration ($\bar{a}$) which is assumed to obtain during the current time step. In this formulation, the piston velocity and displacement are given by

$$V = V_o + \bar{a}\Delta t \tag{3.5}$$

$$X = X_o + V_o\Delta t + \tfrac{1}{2}\,\bar{a}\,(\Delta t)^2 \tag{3.6}$$

where the zero subscripts indicate values at the beginning of the current time step Δt. The actual piston motion is simulated by decreasing the density of the graphite appropriately in the cell interfacing with the UO_2 sample. To avoid unrealistically short time steps, however, an additional time step limitation had to be introduced based on a maximum fraction (0.1) of the total original amount of graphite allowed to be depleted during a single time step.

3.1.4 Global Momentum Model

To provide an upper bound on the predicted piston acceleration, an alternate motion model called the global momentum model was developed. In this model, one assumes that the total increase in sample momentum during a time interval is instantaneously transferred to the piston. The average acceleration is then given by

$$\bar{a} = (M^n - M^{n-1})/\xi A\Delta t^{n-1} \tag{3.7}$$

where M^n is the sample momentum at time step n. This acceleration is used in Eqs. (3.5) and (3.6).

3.1.5 Energy Deposition

As indicated in Ref. 6, a Gaussian temporal variation, shown in Figure 8, of the deposited energy is assumed. The source is neglected beyond three standard deviations in duration. Due to the SIMMER requirement that liquid be present in each mesh cell, the actual mechanistic sample motion was began after 1% of the sample had melted (see Figure 8). Assuming no motion up to that time ($t_{1\%}$) and using the appropriate heat capacity model, one can obtain $t_{1\%}$ by solving a transendental equation. The remainder of the distribution was tabulated and input into the SIMMER-II code as a power distribution. The spatial distribution was also entered in tabular fashion.

3.2 The FARA Code

3.2.1 Code Description

The FARA code was originally designed to solve the finite difference equations arising from two component fluid flow. Since the code is

relatively unknown, we will detail the code operation, including finite difference equations solved, solution algorithm, coding and benchmark problems. The following discussion will be for a one component model only. The FARA code solves the following Eulerian fluid conservation equations in one dimensional plane geometry:

$$\frac{\partial \rho}{\partial t} + \frac{\partial (\rho U)}{\partial z} = 0$$

$$\frac{\partial}{\partial t}(\rho U) + \frac{\partial}{\partial z}(\rho U^2) = -\frac{\partial P}{\partial z} + f\,U^2 \qquad (3.8)$$

$$\frac{\partial (\rho e)}{\partial t} + \frac{\partial}{\partial z}(\rho e U) = -P\frac{\partial U}{\partial z} + s(t)$$

where ρ = density

U = velocity

e = specific internal energy

P = pressure

s = source term.

Coupled with the above equation is an equation of state.

3.2.2 Numerical Solution

The above equations are cast into finite difference equations which form a non-linear algebraic set for the field variables, ρ, U, e, P. The convective terms in the continuity and energy balance equations are approximated by a full donor cell differencing scheme, while the momentum balance equation is approximated by a partial donor cell differencing scheme [19].

The following conventions will be adopted for notational clarity:

(A)
X(1,I) = DENSITY AT CELL I
X(3.I) = VELOCITY
X(5,I) = VOLUME FRACTION (=1.0)
X(7,I) = PRESSURE
X(9,I) = SPECIFIC INTERNAL ENERGY
X(11,I) = TEMPERATURE

Note: The even numbered array values are for second component when required.

BEST DOCUMENT AVAILABLE

B. The mesh scheme is defined by the following diagram:

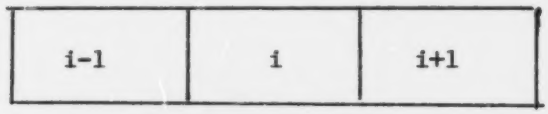

The velocities are cell edged while all other field variables are cell centered. Superscripts refer to time dependence and subscripts refer to spatial dependence. The continuity equations are rewritten after employing the above conventions as follows:

MASS

$$\frac{\rho_i^{N+1} - \rho_i^{N}}{\Delta t} + \frac{1}{2\Delta z_i}\left[\rho_i^{N+1}\left(U_i^{N+1} + |U_i^{N+1}|\right) + \right.$$

$$+ \rho_{i+1}^{N+1}\left(U_i^{N+1} - |U_i^{N+1}|\right) - U_i^{N+1}\left(\rho_{i-1}^{N+1} + \rho_i^{N+1}\right) - \qquad (3.9)$$

$$\left. - |U_i^{N+1}|\left(\rho_{i-1}^{N+1} - \rho_i^{N+1}\right)\right] = 0$$

where

$$\overline{\Delta z_i} = 1/2\ (\Delta z_i + \Delta z_{i+1})$$

MOMENTUM

$$\frac{(\rho U)_{i+1/2}^{N+1} - (\rho U)_{i+1/2}^{N}}{\Delta t} + \frac{1}{\Delta z_1}\left[(\rho U^2)_{i+1}^{N+1} - (\rho U^2)_i^{N+1}\right] - f(U_i^{N+1})^2 +$$

$$+ \frac{1}{\Delta z_i}\left[P_{i+1}^{N+1} - P_i^{N+1}\right] = 0 \qquad (3.10)$$

where

$$(\rho U^2)_i^{N+1} = 1/2\ \rho_i^{N+1}\left[(U_{i+1/2} + U_{i-1/2})Y_{i+1} + \right.$$

$$\left. + (U_{i-1/2} - U_{i+1/2})\ |Y_i|\right]^{N+1}$$

BEST DOCUMENT AVAILABLE

$$(\rho U^2)_{i+1}^{N+1} = 1/2\ \rho_{i+1}^{N+1} \left[(U_{i+3/2} + U_{i+1/2}) Y_{i+1} + \right.$$

$$\left. + (U_{i+1/2} - U_{i+3/2})\ |Y_{i+1}| \right]^{N+1}$$

$$Y_i^{N+1} = 1/2\ (U_{i+1/2} + U_{i-1/2})^{N+1}$$

$$Y_{i+1}^{N+1} = 1/2\ (U_{i+3/2} + U_{i+1/2})^{N+1}$$

$$\rho_{i+1/2}^{N+1} = d_i\ \rho_{i+1}^{N+1} + c_i \rho_i^{N+1}$$

$$c_i = \frac{\Delta z_i}{\Delta z_i + \Delta z_{i+1}}\ ,\ d_i = \frac{\Delta z_{i+1}}{\Delta z_i + \Delta z_{i+1}}$$

ENERGY

$$\frac{(\rho e)_i^{N+1} - (\rho e)_i^N}{\Delta t} + \frac{1}{\Delta z_i} \left[(\rho e U)_{i+1/2}^{N+1} - (\rho e U)_{i-1/2}^{N+1} \right] +$$

$$+ \left[P_i^{N+1} + P_{i+1}^{N+1} \right] \frac{1}{\Delta z_i} \left[U_{i+1/2}^{N+1} - U_{i-1/2}^{N+1} \right] -$$

$$- s^{N+1} = 0 \qquad (3.11)$$

where

$$(\rho e U)_{i\pm1/2}^{N+1} = 1/2 \left\{ \left[(\rho e)_{i\pm1} + (\rho e)_i \right]^{N+1} \cdot U_{i\pm1/2}^{N+1} \mp \right.$$

$$\left. \mp \left[(\rho e)_{i\pm1} - (\rho e)_i \right]^{N+1} \cdot |U_{i\pm1/2}^{N+1}| \right\} .$$

The FARA code employs the multivariate Newton-Raphson technique as the solution algorithm [20]. An iterative procedure is defined for each cell i, such that convergence to the solution of the nonlinear equations is effected through an approach along the gradient of the solution surface mapped out by the field variables. The calculational scheme moves along the mesh grid from left to right with each cell taken in order. The Newton-Raphson iteration at each cell is termed an inner iteration while a sweep through the mesh grid constitutes an outer iteration. For any

BEST DOCUMENT AVAILABLE

particular cell i, knowledge of the downstream advanced time variables is required; however, they currently are unknown. To accommodate this difficulty, these quantities are assumed to have the values of the previous outer iteration and are corrected for in the outer iteration.

In the solution scheme for a single component, the residuals of the finite difference equations describing the flow are represented as follows:

F(1) = mass continuity

F(3) = momentum balance

F(7) = pressure correlation

F(9) = energy balance

F(12) = temperature correlation

If the above equations are solved simultaneously, then the solution is considered to be an implicit solution. However, it is possible to solve for a particular variable at the conclusion of an outer iteration. The solution is then considered to be explicit in that variable. This operation is performed by the use of input switches. One advantage of this feature is a reduction in computational costs.

In the Newton-Raphson solution algorithm, the kth approximation to the true value is obtained via

$$\bar{x}^{k} = \bar{x}^{k-1} - \left[J(\bar{x}^{k-1}) \right]^{-1} \cdot \bar{F}(x^{k-1}) \tag{3.12}$$

where

$\bar{F}(x^{k-1})$ = equation residue vector

$\bar{x}^{k}$ = the array of field variables at the k^{th} iterate

$[J(\bar{x}^{k-1})]^{-1}$ = inversion of Jacobian matrix,

$$J(\bar{x}^{k-1}) = \begin{matrix} \frac{\partial F_1}{\partial x_1} & \frac{\partial F_1}{\partial x_3} & \cdots & \frac{\partial F_1}{\partial x_9} \\ \frac{\partial F_3}{\partial x_1} & \frac{\partial F_3}{\partial x_3} & \cdots & \frac{\partial F_3}{\partial x_9} \\ \frac{\partial F_9}{\partial x_1} & \frac{\partial F_9}{\partial x_3} & \cdots & \frac{\partial F_9}{\partial x_9} \end{matrix} \tag{3.13}$$

BEST DOCUMENT AVAILABLE

Convergence is satisfied when each variable of the kth approximation is within some specified error of the k-1 approximation. Each variable has its own error bounds with a possible 20 inner iterations allowed per mesh cell.

On a cell by cell basis, the calculational scheme is 1) determination of equation residuals F(N), 2) calculations of Jacobian matrix elements, 3) inversion of Jacobian matrix, 4) determination of advanced time variable values and 5) repeat until convergence. The above procedure is repeated for each cell in the mesh (one outer iteration) and a time step is completed when the specified number of outer iterations are performed.

3.2.3 Benchmark Problems

As previously mentioned, FARA was conceived parimarily to test the numerical method. As such, the FARA code was tested and benchmarked for a fast reactor safety application [21]. For the UO_2 experimental analysis, several modifications were necessary, resulting in further testing. The modifications include an energy source and boundary motion. In order to test the code accuracy and programming, several benchmark problems have been devised and will now be discussed.

Energy Source Input

Addition of an energy source is one of the changes required to properly analyze the UO_2 equation of state experiment. Based on the energy pulse data supplied by Benson [6], the energy term would be Gaussian in time with a 0.6 microsec (FWHM) duration. From this we determined

$$s(t) = \frac{A}{\sigma\sqrt{2\pi}} \exp\left(-1/2 \left(\frac{(t-\mu)}{\sigma}\right)^2\right) \qquad (3.14)$$

where

A = total energy deposited (J/g)

σ = standard deviation

$$= \frac{FWHM}{2\sqrt{2+1n2}}$$

$\mu = 3\sigma$.

Note that the source depends on time only with the spatial dependence being neglected.

In order to test the source energy input equation, a no flow, energy addition problem was solved using the perfect gas law for the EOS. The analytical solution to the problem is

BEST DOCUMENT AVAILABLE

$$(e-e_o) = \frac{A}{2}\left[\operatorname{erf}\left(\frac{\mu}{\sqrt{2\sigma}}\right) - \operatorname{erf}\left(\frac{\mu-t}{\sqrt{2\sigma}}\right)\right]$$

for $\mu > t$ (3.15)

$$(e-e_0) = \frac{A}{2}\left[\operatorname{erf}\left(\frac{\mu}{\sqrt{2\sigma}}\right) + \operatorname{erf}\left(\frac{t-\mu}{\sqrt{2\sigma}}\right)\right]$$

for $t > \mu$.

The test problem had a 500 J/g peak energy source. The time step was 5 nsec and there was 140 time steps. Analytical and numerical results are plotted in Figure 9. The comparison is for $\mu > t$ only. There is excellent agreement between FARA's numerical results and those of the analytical solution.

Frictional Flow

This is a duct flow problem that examines the momentum loss due to friction at the walls. This problem was benchmarked for two components in reference 21. The purpose of this problem is to provide an overall check on code integrity, since the frictional loss term is not used in the EOS analysis.

The initial fluid (U_o) is 0.1 m/sec with a frictional coefficient f of 1.0×10^8 kg/m^4. The analytical solution for an incompressible fluid is

$$u = \frac{U_o}{1 + \frac{U_o f t}{\rho}} \qquad (3.16)$$

For this problem, the density was taken to be 1.3 kg/m^3 with a time step of 1 nsec and a total of 50 time steps. The analytical and numerical velocities are shown in Figure 10. The code results are somewhat high but within a reasonable error of 1 percent.

Heat Transfer

A quiescent (no flow) two component heat transfer problem was chosen for a detailed examination of the numerical solution involving heat transfer as compared to the analytical solution. The analytical solution is of the form

$$T_1 = \frac{1}{1 + \frac{\rho_2\beta_1}{\rho_1\beta_2}}\left[T_{10} + \frac{\rho_1\beta_2}{\rho_2\beta_2}\left(T_{20} + (T_{10} - T_{20})e^{-\alpha t}\right)\right] \qquad (3.17)$$

BEST DOCUMENT AVAILABLE

where

$$\alpha = h(\beta_1\rho_2+\rho_1\beta_2)$$

$$T_1 = \beta_1 E_1,\ T_2 = \beta_2 E_2$$

h = heat transfer coefficient

T_{10}, T_{20} = initial temperature

$$T_{10} = 4000K, \quad T_{20} = 1200K.$$

For $h = 10^5$ J/s-m^2 °K, the temperature found in the implicit solution deviated substantially from the exact solution (see Figure 11). The deviation is caused by numerical mass diffusion resulting from an erroneous pressure gradient. When the pressure was found explicitly (at the completion of an outer iteration), the exact solution was reproduced. For both the implicit and explicit solutions three outer iterations were performed. The number of outer iterations was altered to determine if this had any effect. After 30 outer iterations, the implicit solution approached the analytical and the explicit remained unchanged. Thus an explicit formulation when heat transfer is dominant will provide a more accurate result.

Shock Tube

A one component shock tube problem was used as a benchmark to insure that FARA contains no algorithmic inaccuracies when all the constitutive equations are used. The physical situation modeled is a diaphragm rupture between two perfect gases at different densities. Resulting flow is from left to right (higher to lower density). The time step was 10 microseconds and a comparison of analytical to numerical results was made at 0.5 msec. Figure 12 is a plot to density versus time for the shock tube problem. Numerical smoothing causes a loss of detail between the contact surface and the shock front; however, the approximation to the rarefaction is reasonably accurate.

Boundary Motion

By far the most important modification made to the FARA code was the addition of a boundary motion capability. Many ideas were not feasible because of the necessary inversion of the Jacobian matrix in the solution algorithm. The concept chosen focuses on the expansion of a 'ghost' cell due to a pressure gradient and fluid momentum.

Calculations for boundary motion begin at the conclusion of all the outer iterations. The concept is divided into three phases. The first phase is an accounting of mass and energy flowing into the expansion cell. The second phase is the actual expansion. An increase in cell volume is caused by a positive pressure gradient. An acceleration term is

calculated based on the pressure gradient and fluid momentum. From the acceleration, we obtain the boundary velocity and displacement from the equations of motion. The third phase entails determination of the effect of the displacement on the field variables in the cell.

A rarefaction problem was chosen for the benchmark analysis. Here the piston was given a constant velocity of 2 m/sec. The fluid density was 1.3 kg/m^3 and a perfect gas was assumed initially at 273K. The analytical solution for this rarefaction is plotted with numerical results in terms of density versus distance in Figure 13. In this situation, the fluid is described by three regions. Region I is outside the rarefaction, Region II is the rarefaction wave and Region III is the undisturbed fluid. For a piston withdrawing to the right, the analytical solution for each region is [22]:

Region I

$$V = C_o - \frac{\gamma-1}{2} u_p \ , \quad \gamma = C_p/C_v$$

with $C_o = \sqrt{RT}$ (3.18a)

Region II

$$V = \frac{\gamma-1}{\gamma+1} \left(\frac{-x}{t} + \frac{2C_o}{\gamma-1}\right) \tag{3.18b}$$

Region III

$$V = C_o \tag{3.18c}$$

and for any region

$$\rho = \rho_o \, (V/C_o)^{2/(\gamma-1)} \tag{3.18d}$$

The results are encouraging but for large piston velocities inaccuracies may be produced. FARA does smooth out the rarefaction wave as expected (Region II) but maintains integrity in Regions I and III.

3.3 The VIOLET Code

3.3.1 Code Description

The VIOLET code was originally developed for laser fusion applications. The fluid flow conservation equations are solved in Lagrangian form thus treating the flow front exactly. Included in the formulation is the usual shock smearing formulation where an additional pressure component is introduced to account for a traveling shock. The equations are solved explicitly using a leap-frog time differencing technique. The differencing scheme is essentially accurate to second order in the time interval. A disadvantage of the Lagrangian formulation is its inability to treat the relative motion of the liquid and vapor phases.

BEST DOCUMENT AVAILABLE

3.3.2 Analytical Benchmark

To provide confidence in the VIOLET solution algorithm a comparison with an adiabatic blowoff was made. Initially a polytropic perfect gas contained in the half space $x \leq 0$ with unit density and pressure is allowed to expand freely. The analytical solution is

$$V = \frac{2C_o}{\gamma+1} \left(\frac{x}{C_o t} + 1\right), \quad \gamma = 5/3 \tag{3.19}$$

and a comparison at several times is shown in Figures 14a-c. Relatively adequate agreement for the present purpose is obtained.

3.4 Inter-code Comparison

In the Table 2 the various modeling features of the three codes used in the experimental analysis are summarized.

To provide further confidence in the operation of the three codes an inter-code comparison was performed. The problem chosen for this comparison is one in which the temperature in the boundary cells of a one-dimensional pipe is instantaneously increased from 273°K to 400°K. Figure 15 shows the position of the peak density of the density wave as it moves toward the center of the pipe. Good agreement between the three codes is seen; however, in the SIMMER-II treatment, a substantial spreading of the material wave due to artificial diffusion is seen from Figure 16. This artificial diffusion also occurs in the FARA formulation. In general, the rather good agreement between the codes lends confidence to the experimental analysis to follow.

4. RESULTS AND DISCUSSION

The comparison of the experimental results with the analysis provided by the three hydrodynamic codes referred to previously will be the subject of this section. Each code comparison will be detailed separately with an overall comparison presented at the end of the section.

4.1 SIMMER-II Analysis

Due to budgetary considerations, the SIMMER comparison concentrated only on the case for which an amount 2030 J/g of specific energy was deposited in the sample. From Figure 17, which shows the piston velocity comparison, a large disparity is noted. These results were obtained with the SIMMER EOS and model 2 for the heat capacity.

To help discuss the results and provide plausible reasons for the large discrepancy, the motion of the graphite piston has been characterized by three time scales--initial acceleration, intermediate motion and long time motion.

4.1.1 Initial Acceleration

Based on the electron beam heating of gold performed in some earlier experiments [23], it has been asserted that the initial sharp increase in piston velocity is due to thermal expansion of the solid fuel. In the following simplified analysis, evidence is provided to indicate that thermal expansion of the solid phase may not account for the experimentally observed initial velocities. Thermal expansion can be separated into three individual components--thermal expansion of the solid particles, thermal expansion of the liquid and expansion upon melting. An incremental piston displacement dz can be related to a temperature increase dT by

$$dz = \frac{\alpha \ell}{2} dT \tag{4.1}$$

where ℓ is the initial sample thickness and α is the coefficient of thermal expansion. The incremental temperature change is related to an incremental time change dt by

$$dT = \frac{\hat{p}}{C_p} dt \tag{4.2}$$

with $\hat{p}$ being the specific power deposited in the sample and C_p the sample heat capacity, thus from Eqs. (4.1) and (4.2)

$$\frac{dz}{dt} = v = \frac{\alpha \ell \hat{p}}{2C_p} \tag{4.3}$$

This result also holds for the liquid phase with α adjusted accordingly. For the liquid phase produced via melting, we have

$$v = \frac{\beta \ell \hat{p}}{2h} \tag{4.4}$$

where β is the fractional volume change upon melting (~ 0.11) and h is the heat of fusion. The values of the thermophysical properties required are given in reference 24. Since the expansion into the void volume between particles is not taken into account, the above analysis will overestimate the velocity due to thermal expansion, and therefore the values should be considered an upper bound. The maximum velocity given by Eq. (4.3) evaluated for the solid and liquid phases and Eqs. (4.4) for the melted liquid is shown in Table 3. These velocities are less than 10% of those observed indicating that expansion alone cannot explain the initial acceleration. A possible explanation for the observed velocities is the release of entrained gas which is discussed later. Also the possibility of "liquid sloshing", where the liquid imparts momentum to the piston due to initial motion on melting, has been addressed by the SIMMER analysis. From Figure 18, however, it is seen that the liquid velocity during the initial acceleration seems not to be large enough to account for the observed velocities.

4.1.2 Intermediate Motion

In this time frame, the vapor pressure of the UO_2 has been assumed to be entirely responsible for the piston motion. The SIMMER analysis, however, indicates that spatial effects may also influence the piston motion during this time. Figure 19 shows the spatial distribution of the pressure as determined by the SIMMER code. The initial pressure gradient is due to ths spatial variation of the energy deposition distribution. At 4μs, pressure equalization is seen to begin from the center outward, but a significant gradient still exists until 15 μs. The existence of a time varying pressure gradient within the sample indicates that considering the piston motion to be due only to a single pressure is an over-simplification. Thus identifying a single pressure with an energy or temperature as was done in the e-beam experiments may not be justified.

4.1.3 Long Time Motion

The long time motion begins at about 15 μs when additional piston acceleration is observed in the experimental data. This acceleration is not predicted by the SIMMER calculation. Benson has attributed the observed acceleration to random measurement error; however, the oscillatory deviation from the straight line fit appears to be systematic as shown in Figure 20 for the 2030 J/g and 3050 J/g cases. The following analysis indicates that the deviation at 15 μs could be due to a liquid wave impacting the piston.

Following the initial fluid impact, at approximately 1 μs, the liquid will reflect off of the piston. If it is assumed that the collision is elastic, the liquid speed will remain unchanged. Traveling at that constant velocity, the liquid will impact the opposite piston at about 13 μs. The impact location is based on the piston displacement data from Reference 6. For the 3050 J/g case, the same analysis indicates liquid impact at 2.5 μs. These times seem to correspond with observed upward trends in the data points. The calculated impact times are 1.2 μs earlier than observed with the delay possibly due to frictional effects which will reduce the wave velocity. If the liquid wave does contribute to the piston motion then identifying the vapor pressure from just the piston acceleration is not valid.

4.1.4 Variation of EOS

The analysis presented thus far has used the SIMMER-II EOS model [10]. In order to evaluate the sensitivity of the results to the EOS model, the Benson dynamic EOS was incorporated in the SIMMER code. Only a 55% velocity increase over the case with the SIMMER EOS is seen while the temporal variation remains the same. It seems, therefore that the dynamic EOS cannot explain the entire discrepancy.

4.1.5 Sensitivity to the Initial UO_2 Density

Since a relatively large error (50-80%) is associated with the initial urania density, a sensitivity study on initial density was performed.

From Table 4, a relatively strong dependency of the velocity on initial density is apparent. Since the sample area density is known, density variations cause the sample thickness to change and the magnitude and timing of the acceleration from the liquid slosh will vary. As shown in the table, the velocities for the 2030 J/g case can be smaller than for the 1990 J/g case due to the uncertainty in the initial density giving a possible explanation for lower observed velocities for the 2030 case than for the 1990 case (see Figure 4).

4.2 FARA Analysis

Numerical velocities calculated using Benson's EOS [6] with heat capacity model 1 are compared to the experimental velocity fits for three energy pulses in Figure 21-23. For the 1860 J/g and 1990 J/g pulses, the slope of the numerical case matches closely with the slope of the experimentally fit line. The obvious difference in each case is due to the initial acceleration. The 2030 J/g pulse results are not as close as the two previous cases. There is a detectable difference in slope, indicating a different vapor pressure.

It would appear that the numerical results bear out the dynamic C_p hypothesis. Taking a closer look, however, this is not the case. The spatial energy deposition for the FARA code energy input is constant. This does not compare to the actual spatial deposition of Figure 3. The addition of a comparable spatial energy deposition would cause a more rapid initial acceleration followed by a gradual leveling of the velocity profile. Numerical results from the FARA code, as with SIMMER, show definite pressure gradients, even though the slope of the velocity are similar to the experimental fit. If this is the case, it is not possible to predict a single vapor pressure in the sample.

4.3 VIOLET Analysis

The results of the analysis using the Lagrangian code VIOLET are presented in Figure 24-27 for the 2030 J/g case. Figure 24 shows the velocity of the lighter piston as determined from the Benson EOS and Model 1 for the heat capacity. As with the SIMMER calculation, the velocities are well below those observed. In addition, the transient nature of the pressure at the UO_2-graphite interface is readily apparent from Figure 25. The Menzies EOS with Model 2 for the heat capacity is used to determine the velocities in Figure 26. As expected, the velocities are lower than predicted with the Benson EOS. Finally, in Figure 27, the asymmetric nature of the piston motion is shown by the differing distances and velocities of the two pistons at the end of 20 μs. Even with the experimental asymmetry there seems to be no irregularities associated with the internal motion of the sample.

5. DISCUSSION OF RESULTS

As seen from Figure 28 in which the results of the experimental analysis are compared to the experiment itself, generally poor agreement is noted. Several possible reasons for the lack of agreement can be formulated including

(a) extraneous pressure sources are contributing significantly to the total pressure

(b) the models embodied in the analysis codes do not adequately describe the physical phenomena associated with the experiment.

5.1 Possible Additional Pressure Sources

Non-fuel vapor pressure sources could arise from impurities in the fuel due to the fabrication process, fuel contamination resulting from atmospheric exposure and carbon monoxide formation. Some common fuel impurities are shown in Table 5. In addition, fission gas release experiments performed at HEDL have indicated the non-fission gas release shown in Table 6 from which a twofold increase in the release upon melting is observed. The pressures associated with these impurities are depicted in Figure 29 along with the band of available pressure data for urania without impurities. In this comparison, it is apparent that at the temperature of interest (~5000°K) the impurities can contribute significantly to the overall pressure. The type and quantity of impurity in the sample used by Benson is unknown and therefore could constitute a large experimental uncertainty.

Another source of pressure could be from water vapor or gases which have been absorbed by the powdered sample during preparation. Results from the VIPER [26] experiments on unirradiated mixed oxide fuel indicate that significant quantities of contaminant gases are released within milliseconds of the power pulse thus adding to the measured pressure.

Another possible pressure source could be the formation of CO from absorbed carbon during handling and/or from the UO_2-graphite piston interface. In fuel disruption experiments currently being performed at Sandia [27] the pressure from CO is thought to be the primary cause of the observed fuel disruption.

As further evidence to support the argument of extraneous pressure sources, Breitung [25] has noted that cooling of the liquid resulting from vapor production should accompany the large volume expansion of the e-beam experiments. In this case, a drop in vapor pressure as seen in the experimental analysis, should also be observed. Since the observed pressure appears constant in time, it cannot be due entirely to the UO_2 vapor. In addition, the simple analysis in §4.1.1 indicates the possibility of a large pressure, not due to thermal expansion, occurring at melting which could be the result of released gases.

5.2 Modeling Uncertainties

Uncertainties in the model parameters and the absence of crucial models could also account for the discrepancy between experiment and analysis. Since rather diverse models yielding relatively similar results have been used, the hydrodynamic model in our estimation is less suspect than the

thermodynamic model. In the future, however, as better models are developed they should be applied to the e-beam experiments in order to resolve the discrepancies.

5.3 Summary

In summary, therefore, three analysis codes with different hydrodynamic models have been applied to the e-beam experiments giving relatively similar results which differ greatly from the experimental observation. There exists enough experimental uncertainty to suggest that the observed pressure could have resulted from a non-fuel vapor source.

Table 1 Sample Thicknesses

Run Number	E (J/g)	Area Density (Kg/m^2)
1	1860	0.12
2	1990	0.12
3	2030	0.12
4	2490	0.25
5	3030	0.25

Table 2 Features of Codes

Feature/Code	SIMMER	FARA	VIOLET
Eulerian formulation	Y	Y	N
Lagrangian formulation	N	N	Y
Implicit algorithm	Y	N	N
Multicomponent treatment	Y	Y	N
Two dimensions	Y	N	N
Two-phase flow	Y	Y	N
Shock following	N	N	Y
Boundary motion	Y	Y	Y
Heat transfer	Y	Y	N
Spatial energy deposition	Y	N	Y

Table 3 Estimated Maximum Velocities from Thermal Expansion

Energy Deposition (J/g)	Velocity (m/s)
1860	9.6
1990	10.3
2030	10.4
2490	26.0
3030	33.0

Table 4 Piston Velocities

Energy Deposition (J/g)	Velocity at 20 μs (m/s)
1860 (nominal)	19.0
1990 (nominal)	29.0
2030 (low dens)	28.6
2030 (nominal)	33.1
2030 (hi dens)	26.9

Table 5 Admissible Contents in LMFBR Fuel Impurities which can Give Rise to Pressure Contributions in an EOS-Experiment [25]

Element	Source
C	hydrocarbon binder
Cl	UF_6
F	
Total H_2 (H_2+H_2O)	sintering atmosphere, air, pellet grinding
N_2	sintering, air

Table 6 Non-Fuel Vapor Gas Release [25]

Maximum Fuel Temperature [°C]	Gases Released (N_2, H_2, CO) [µmol/g]
1700	9.8
2100	8.4
2420	13.9
2700	13.0
fuel melting temperature	24.0
fuel melting temperature	23.6

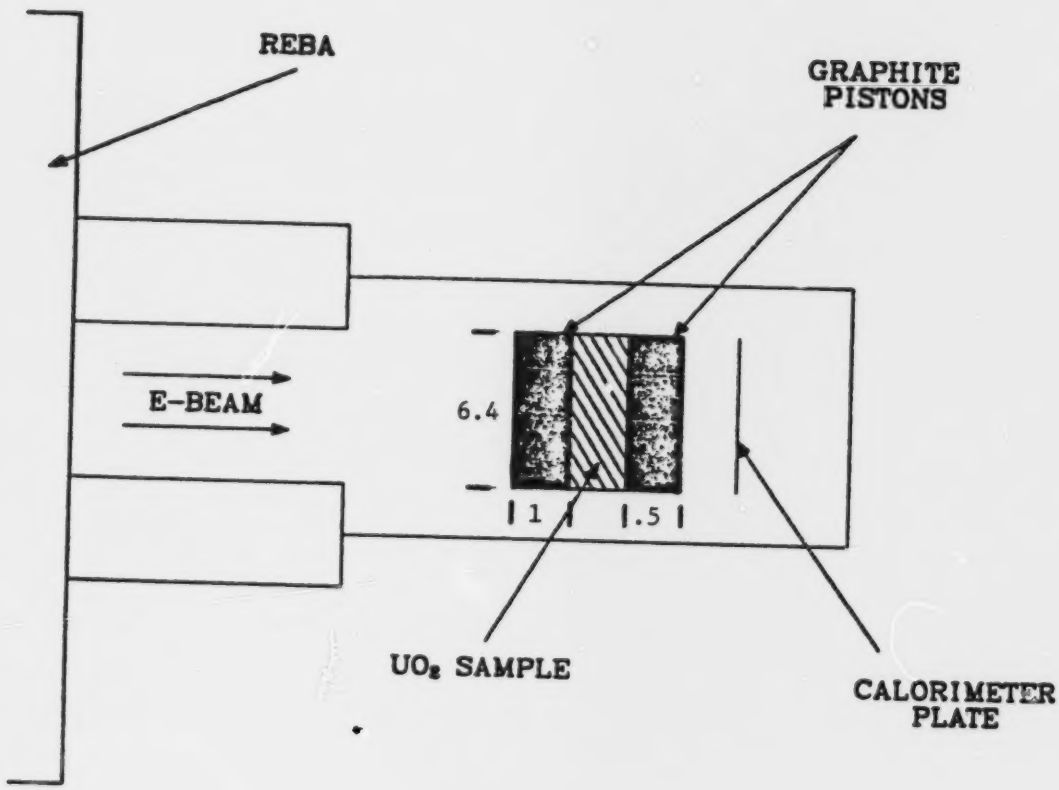

Figure 1 Experiment Schematic (Dimensions in mm)

BEST DOCUMENT AVAILABLE

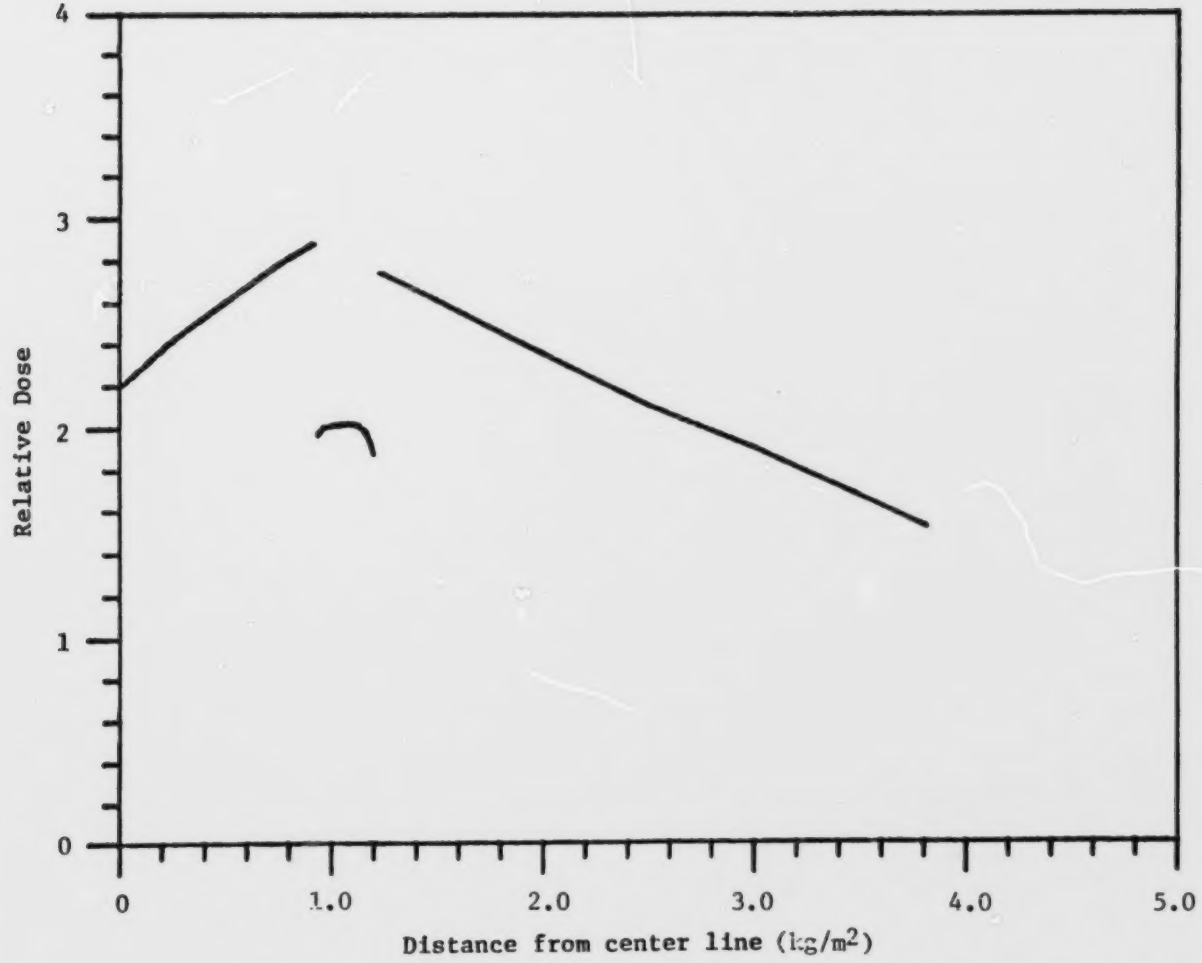

Figure 2 Spatial Variation of the Energy Deposition

BEST DOCUMENT AVAILABLE

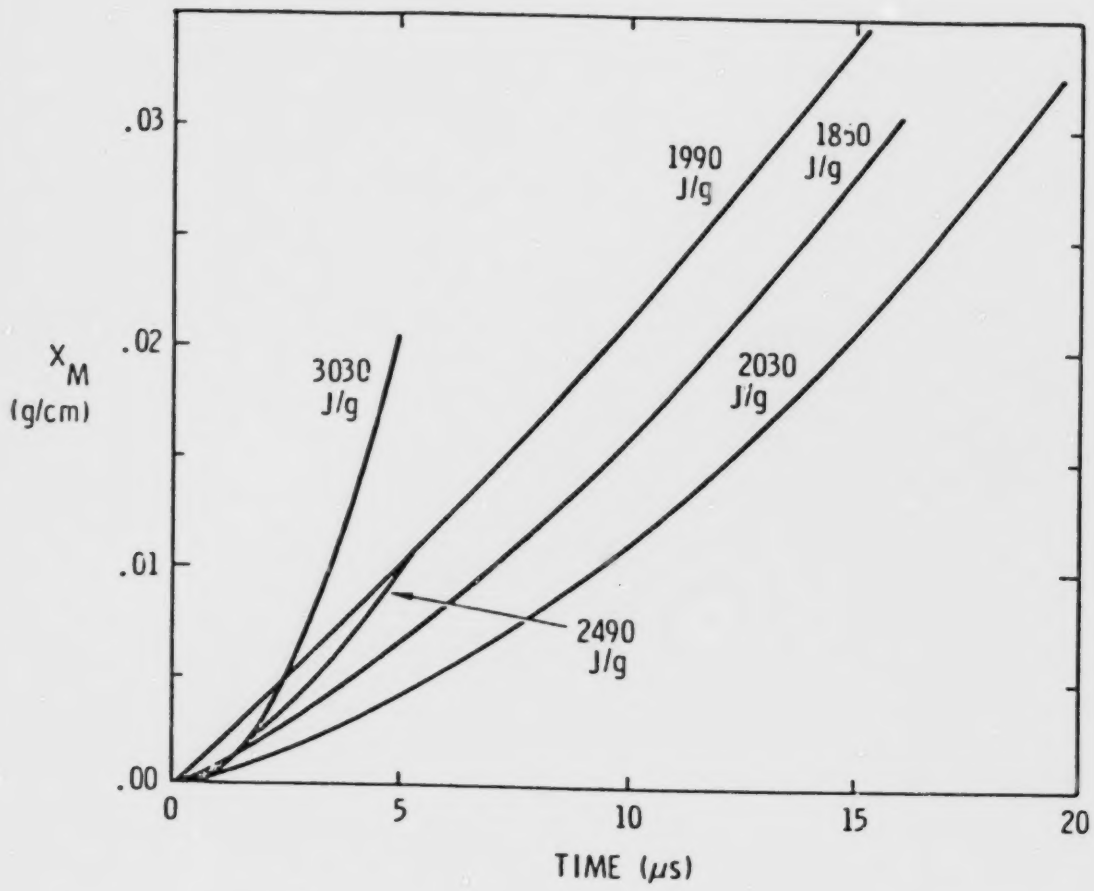

Figure 3 Piston Displacement Variation with Energy Deposition

BEST DOCUMENT AVAILABLE

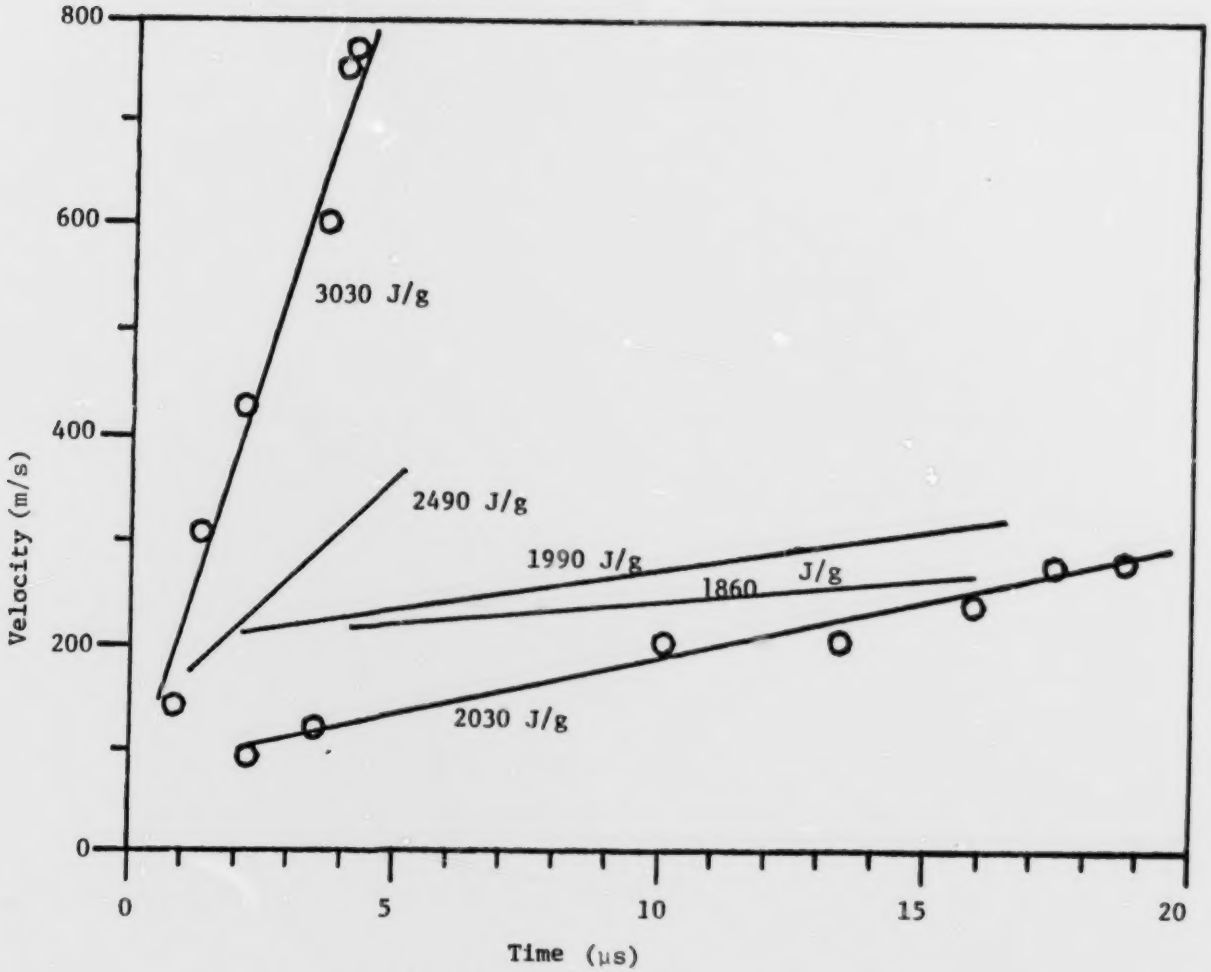

Figure 4 Piston Velocity Variation with Energy Deposition

BEST DOCUMENT AVAILABLE

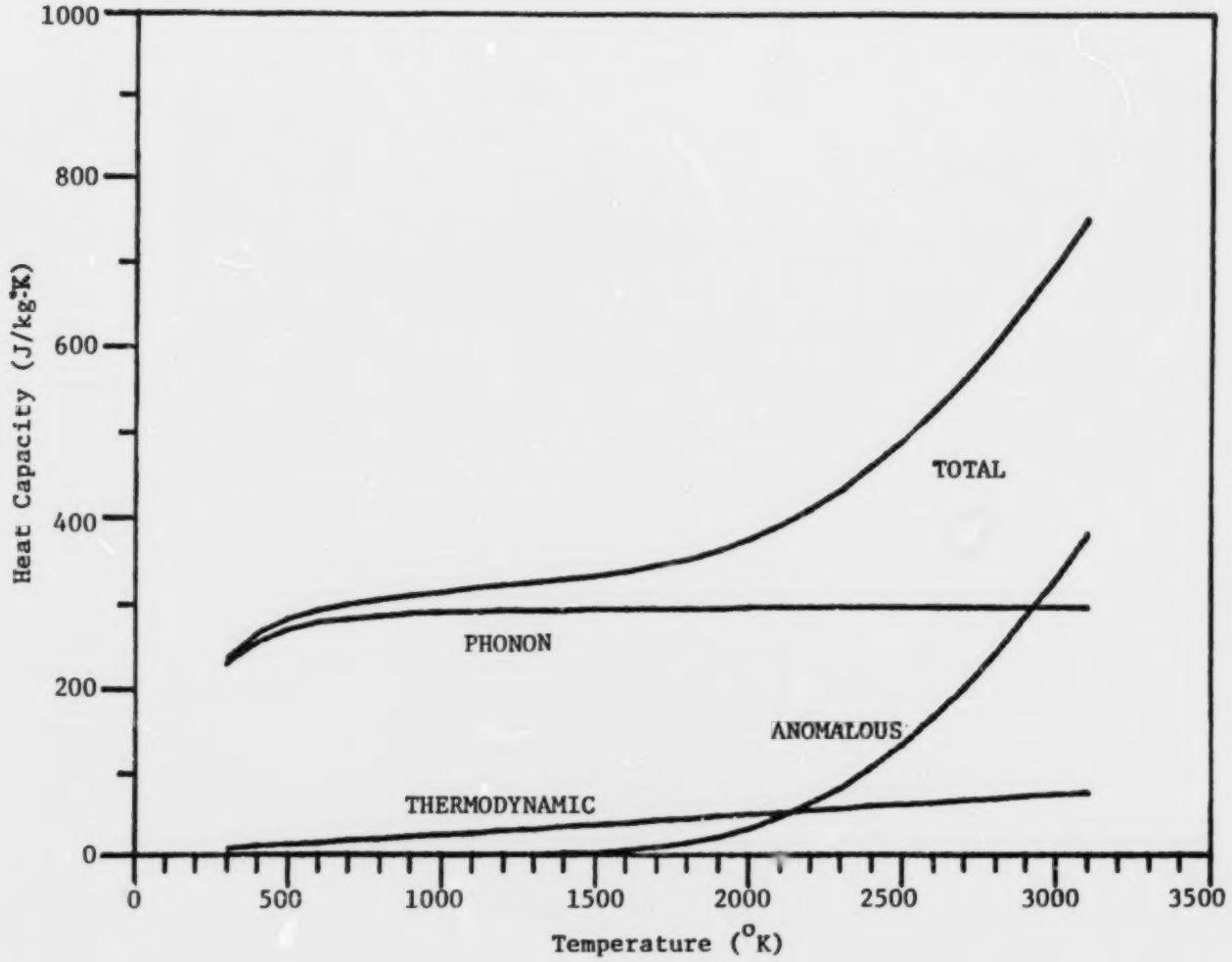

Figure 5 Solid UO_2 Heat Capacity [8]

BEST DOCUMENT AVAILABLE

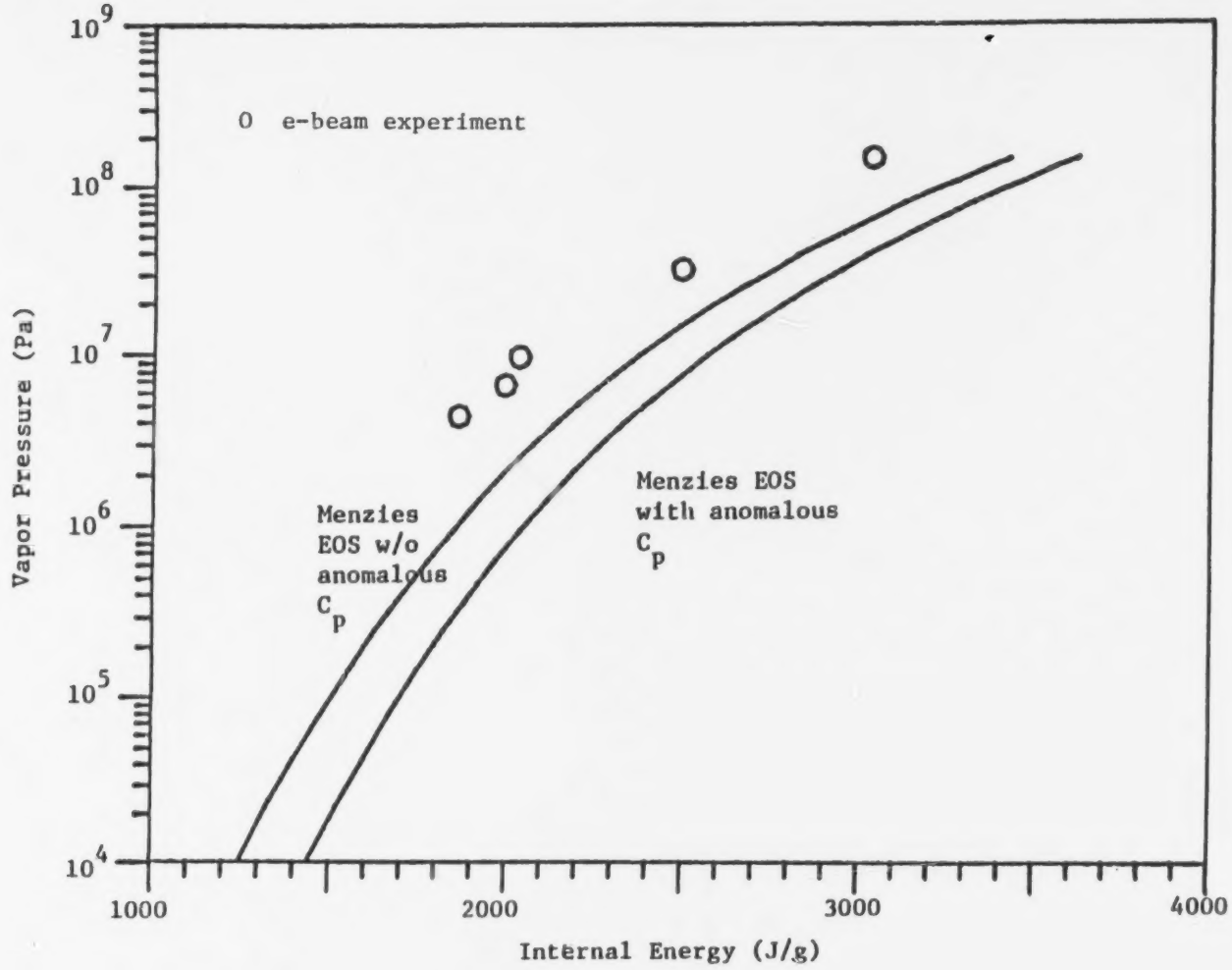

Figure 6 EOS in Pressure-Energy Format

BEST DOCUMENT AVAILABLE

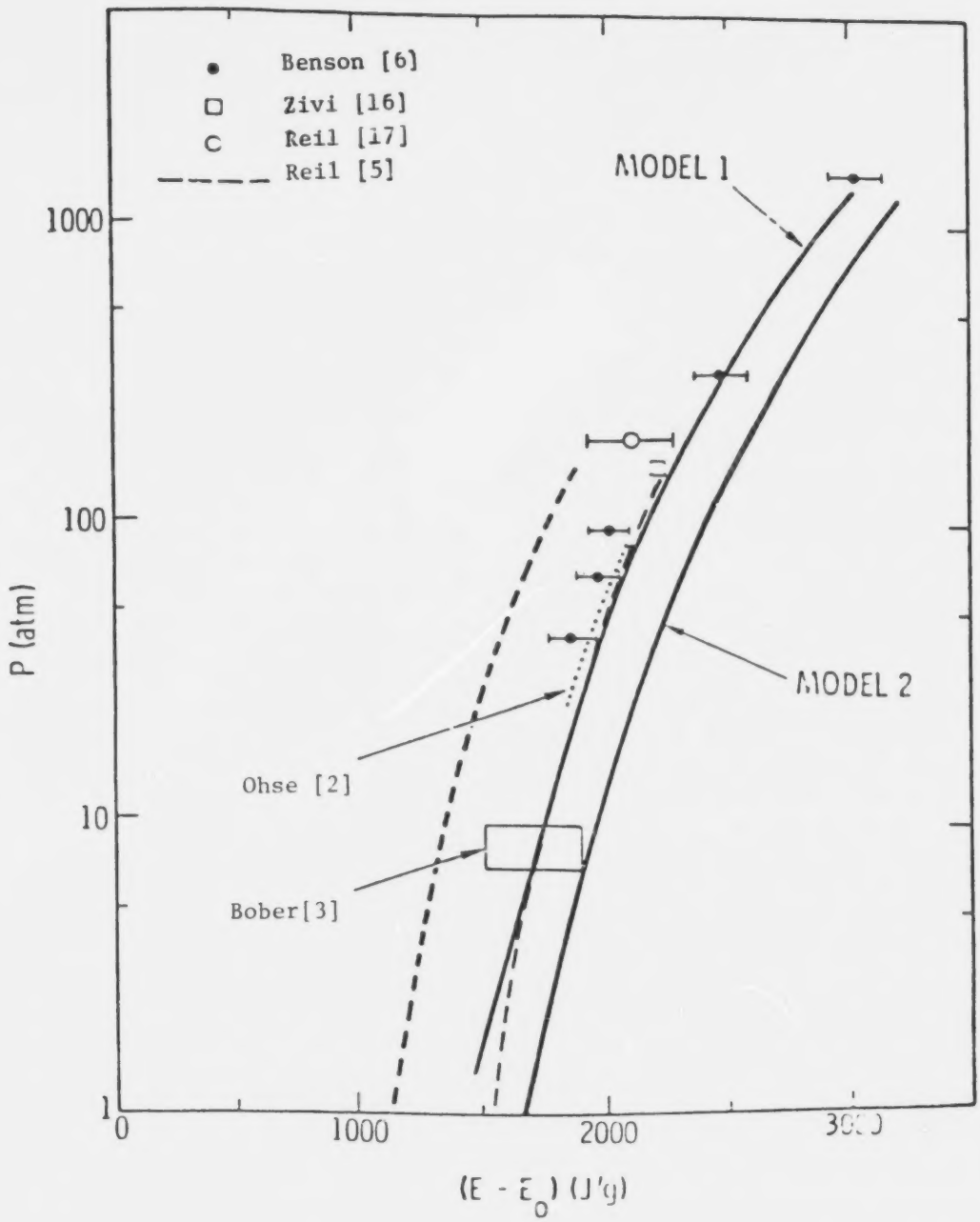

Figure 7 Comparison of e-beam Results with Other Data

BEST DOCUMENT AVAILABLE

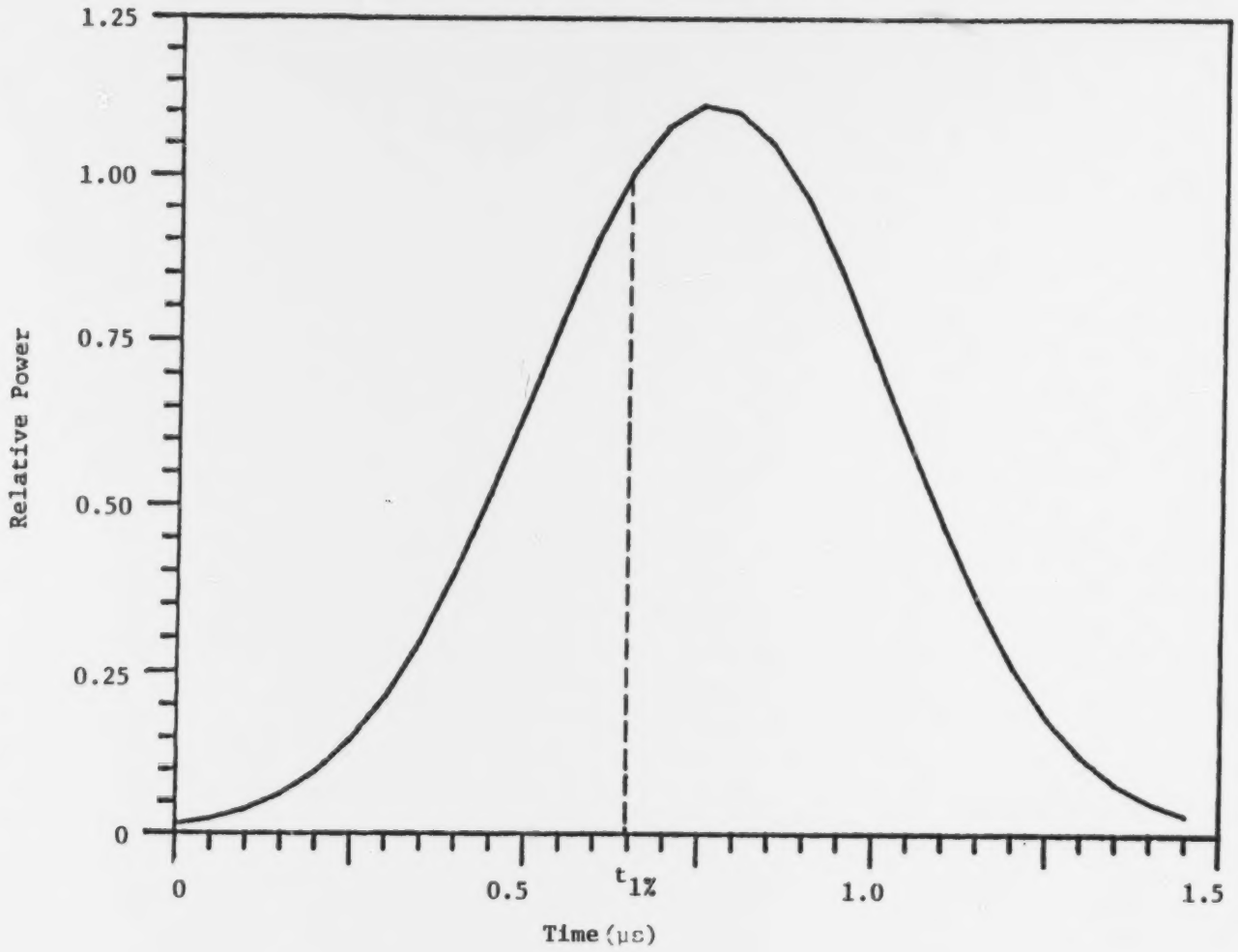

Figure 8 Normalized Source Variation in Time

BEST DOCUMENT AVAILABLE

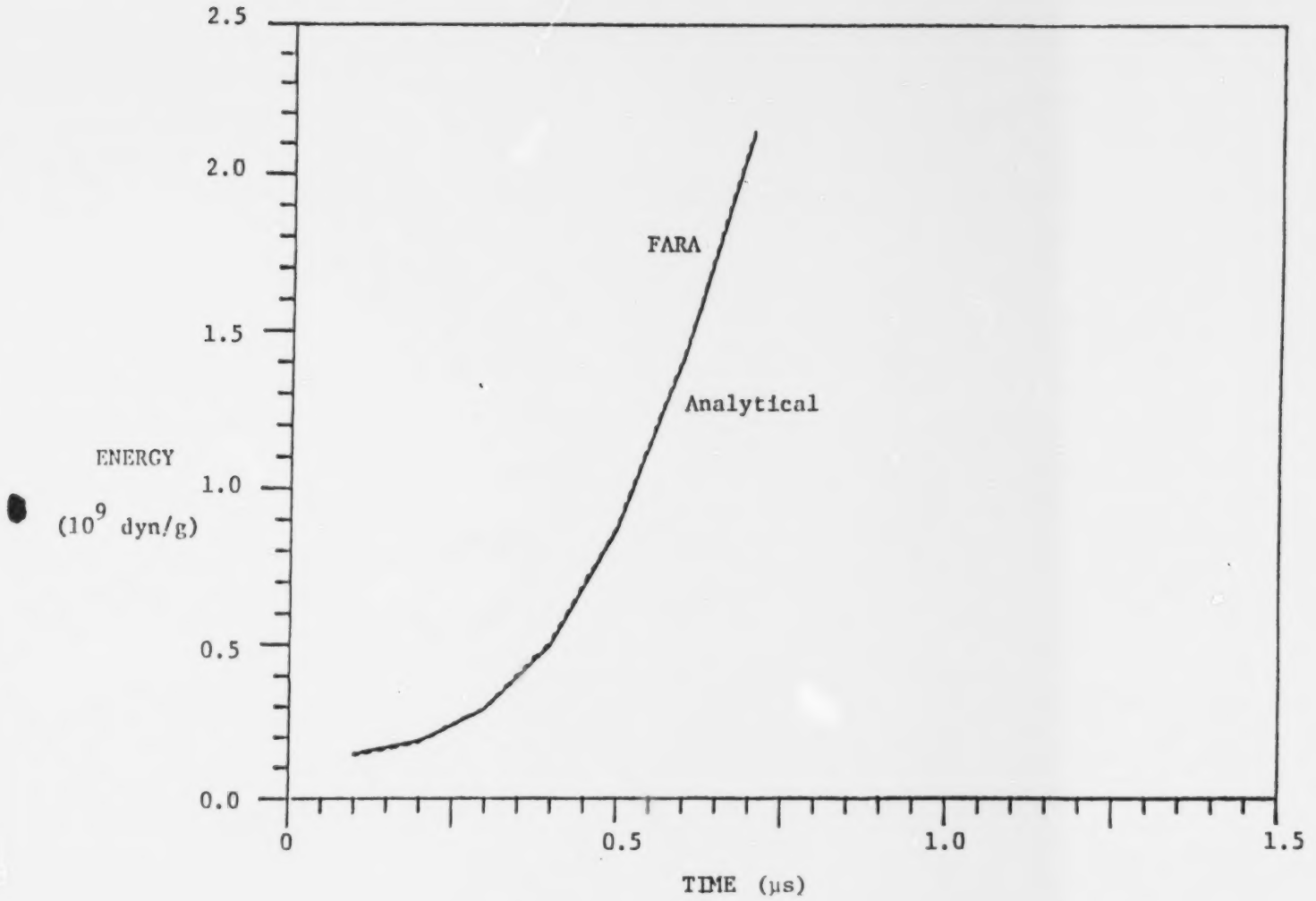

Figure 9 Energy Input Benchmark

BEST DOCUMENT AVAILABLE

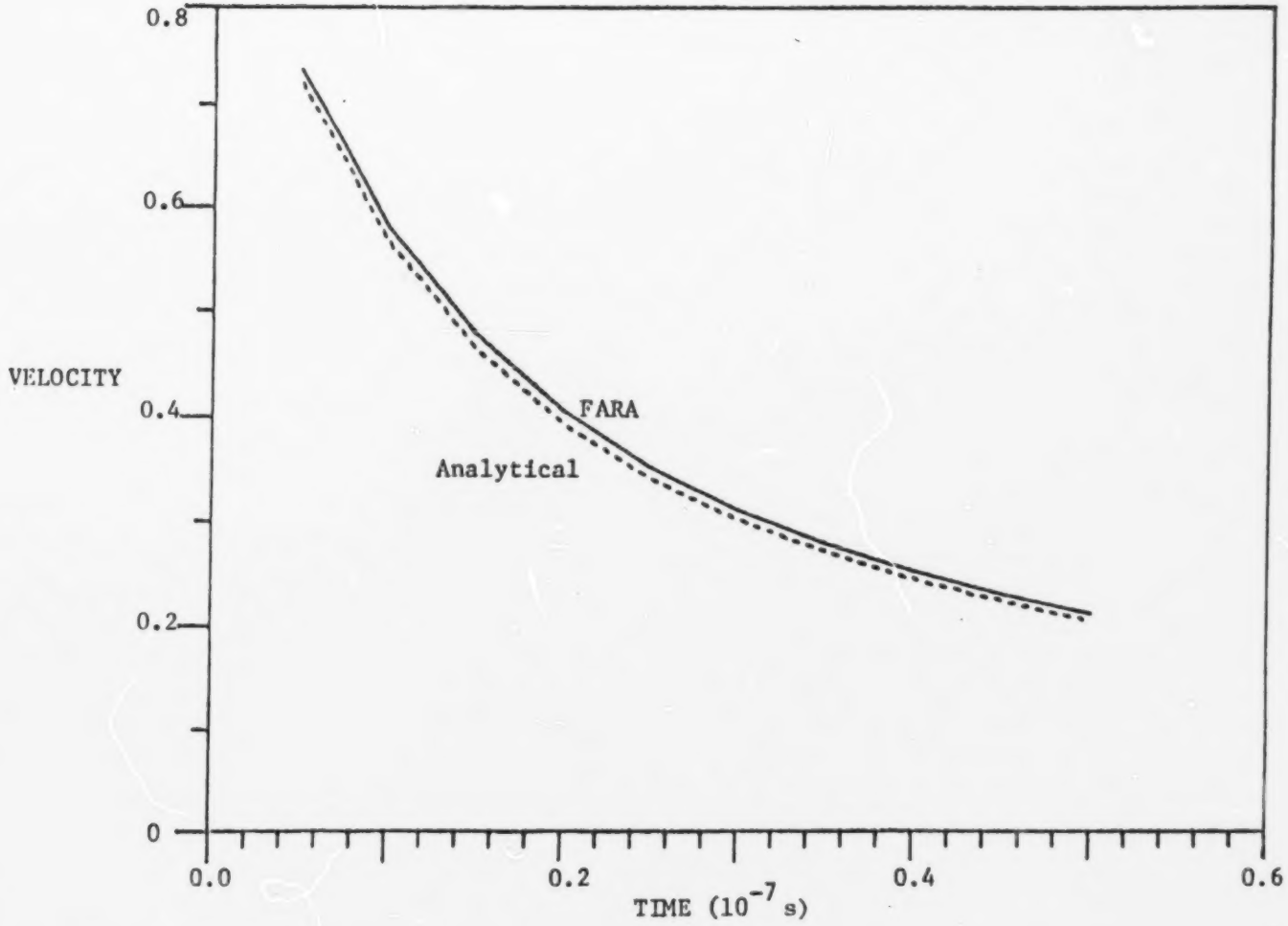

Figure 10 Frictional Flow Benchmark

BEST DOCUMENT AVAILABLE

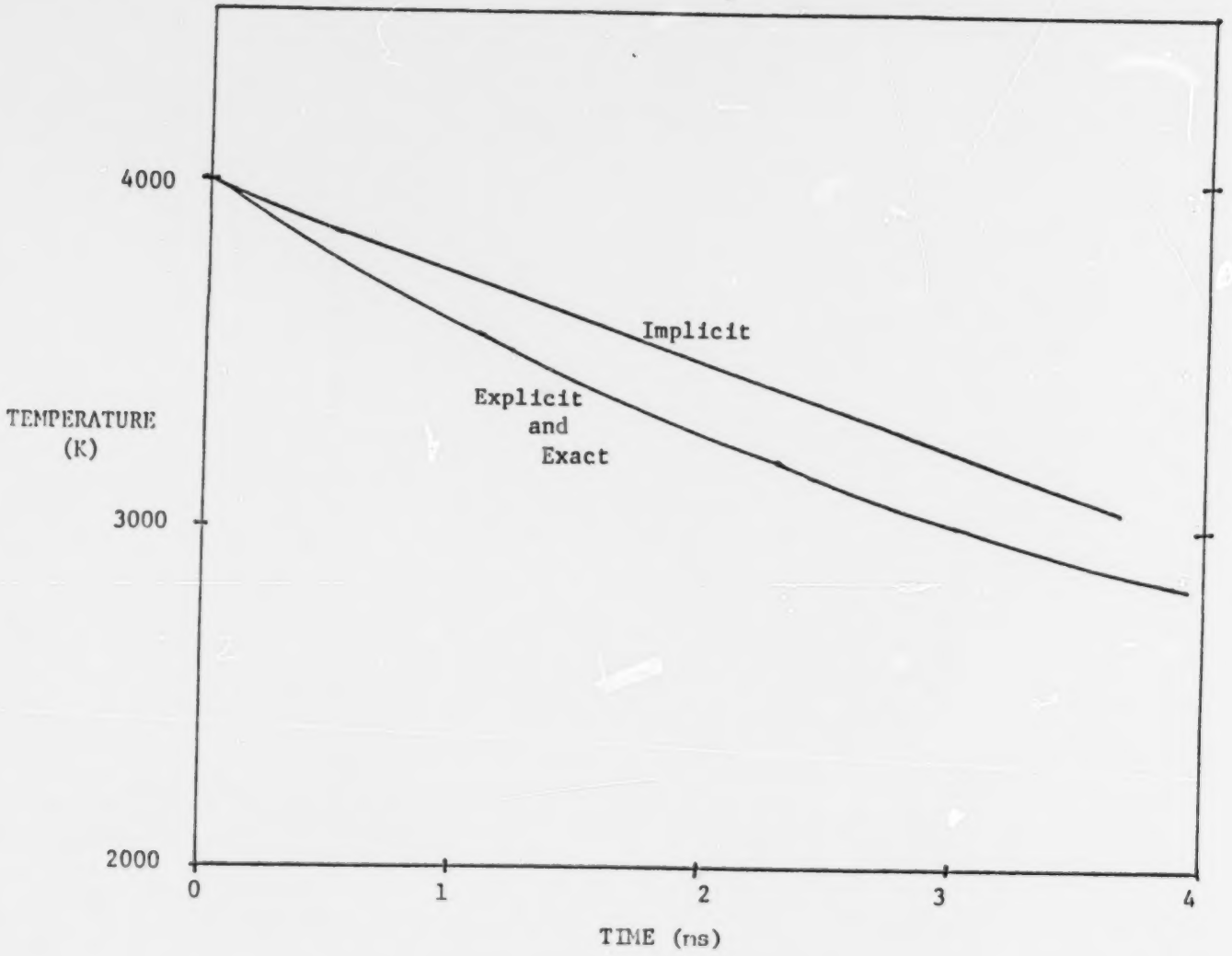

Figure 11 Heat Transfer Benchmark

BEST DOCUMENT AVAILABLE

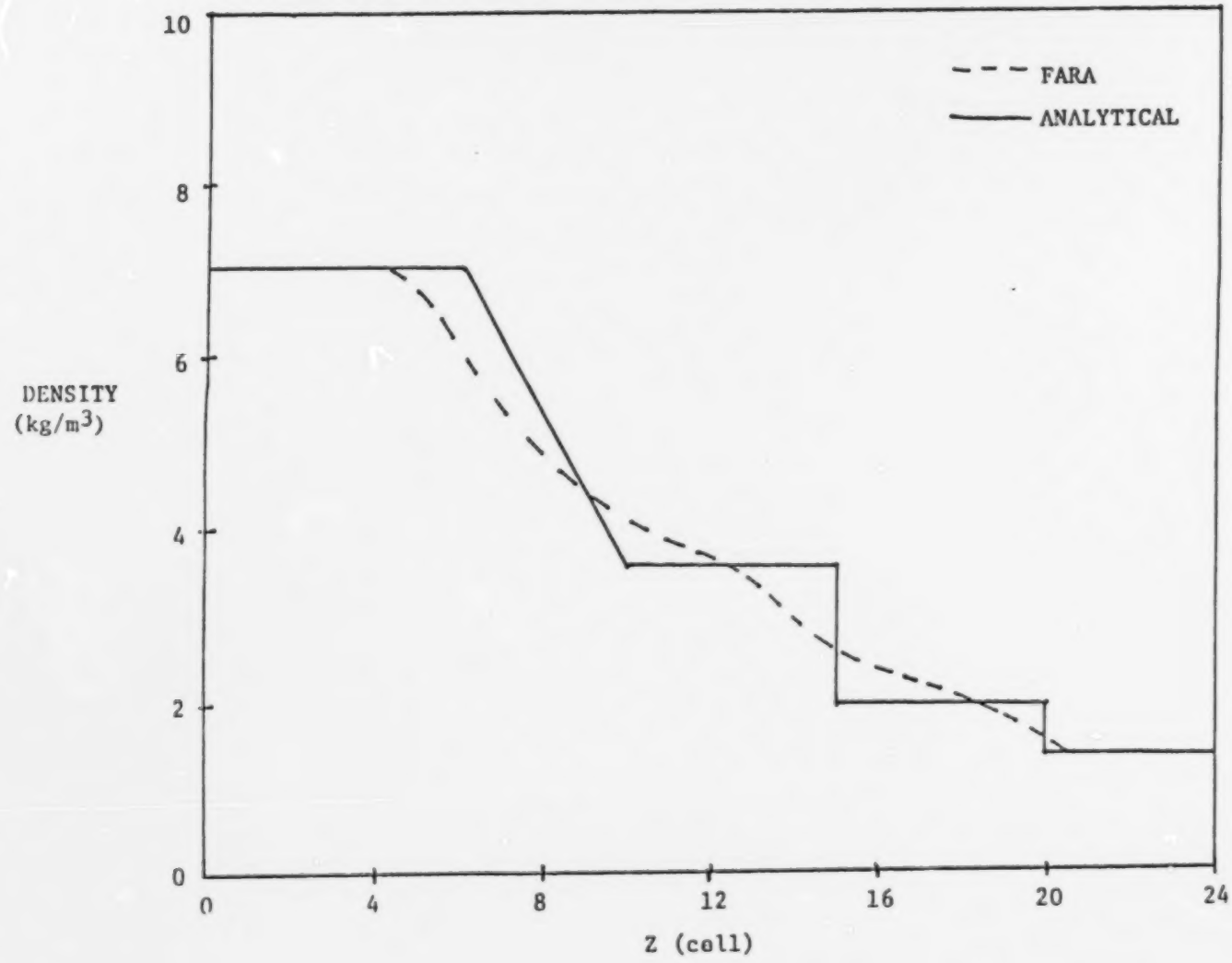

Figure 12 Shock Tube Benchmark

BEST DOCUMENT AVAILABLE

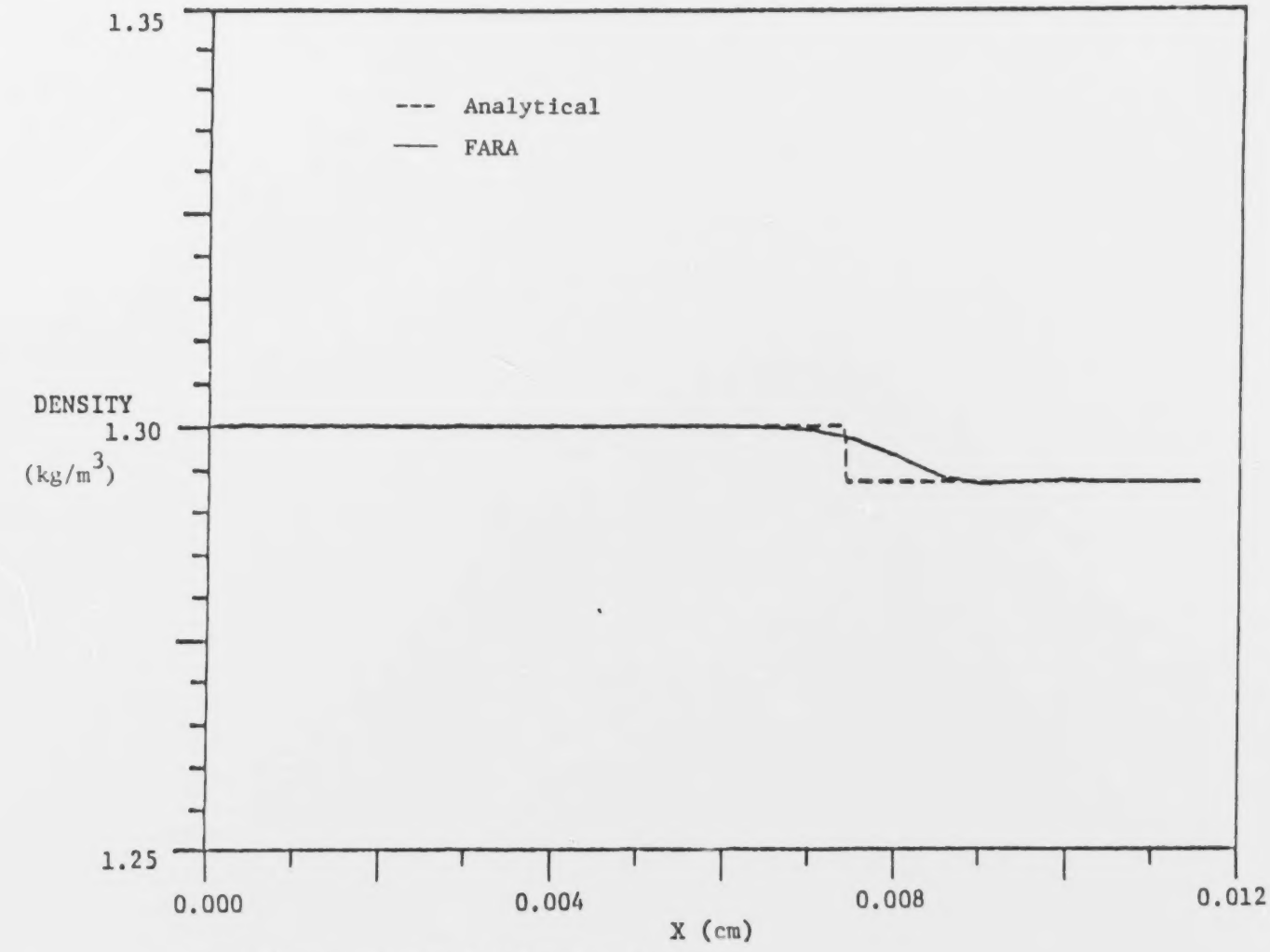

Figure 13 Rarefaction Benchmark

BEST DOCUMENT AVAILABLE

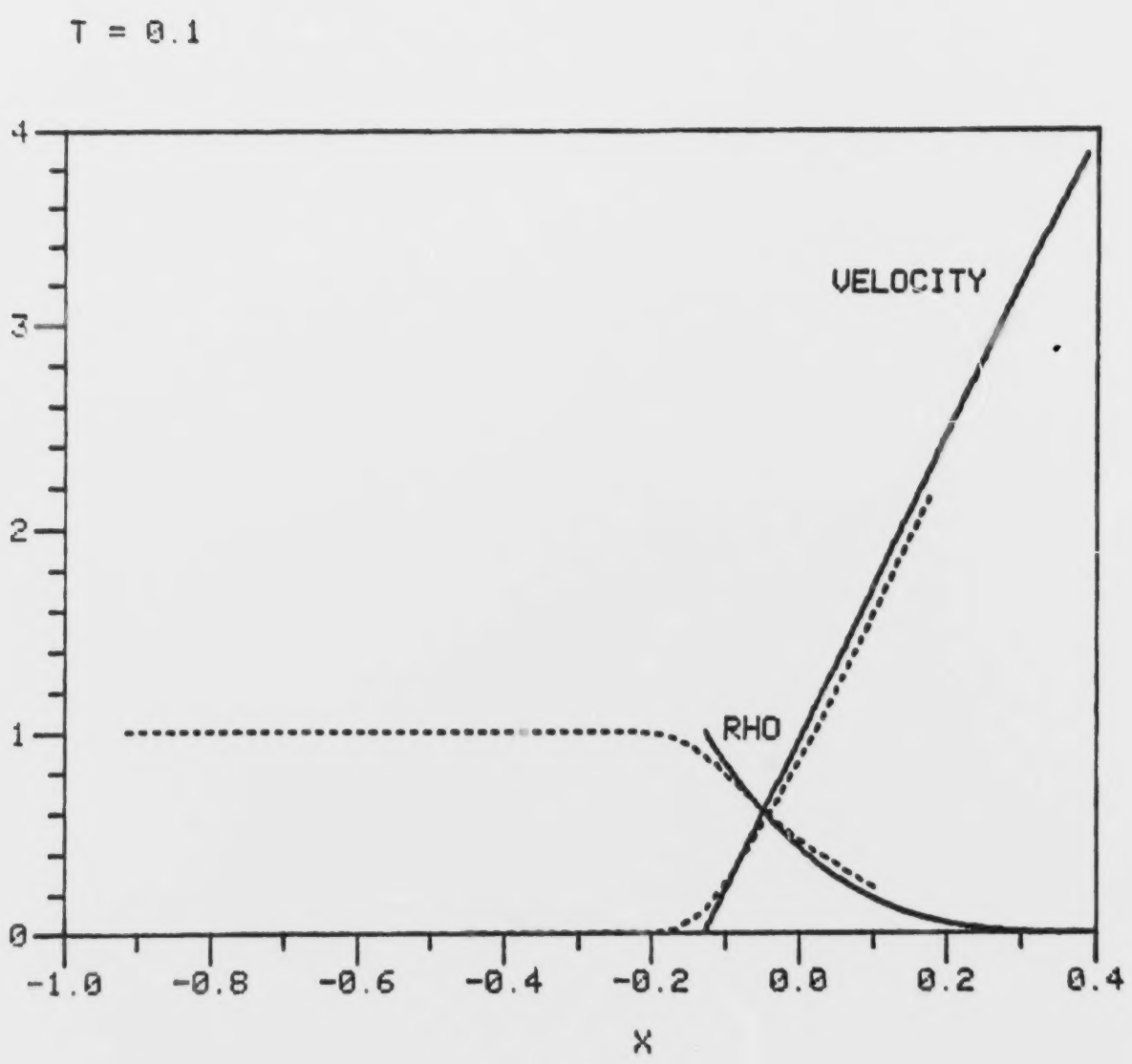

Figure 14a Adiabatic Blowoff Benchmark

BEST DOCUMENT AVAILABLE

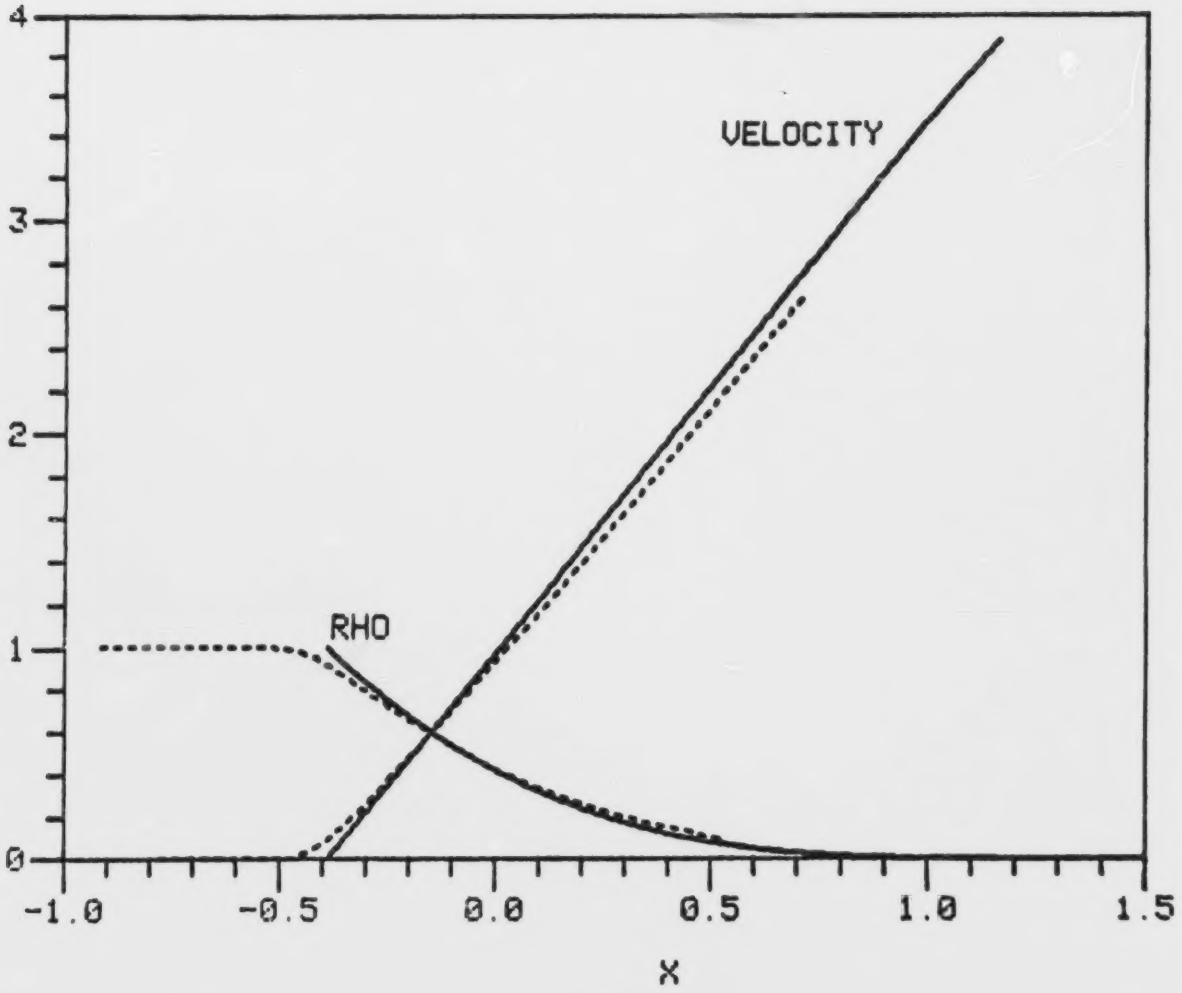

Figure 14b Adiabatic Blowoff Benchmark

BEST DOCUMENT AVAILABLE

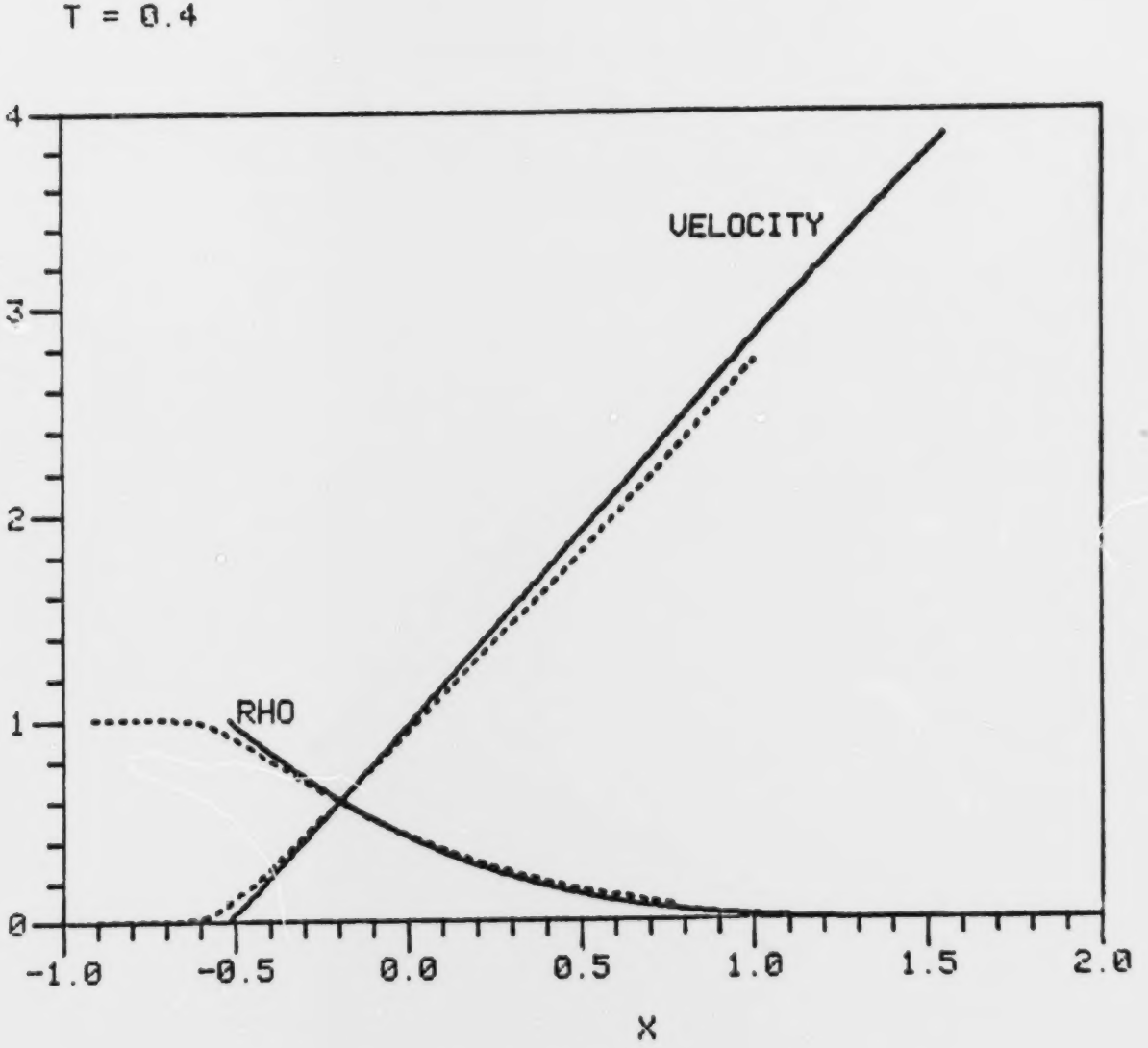

Figure 14c Adiabatic Blowoff Benchmark

BEST DOCUMENT AVAILABLE

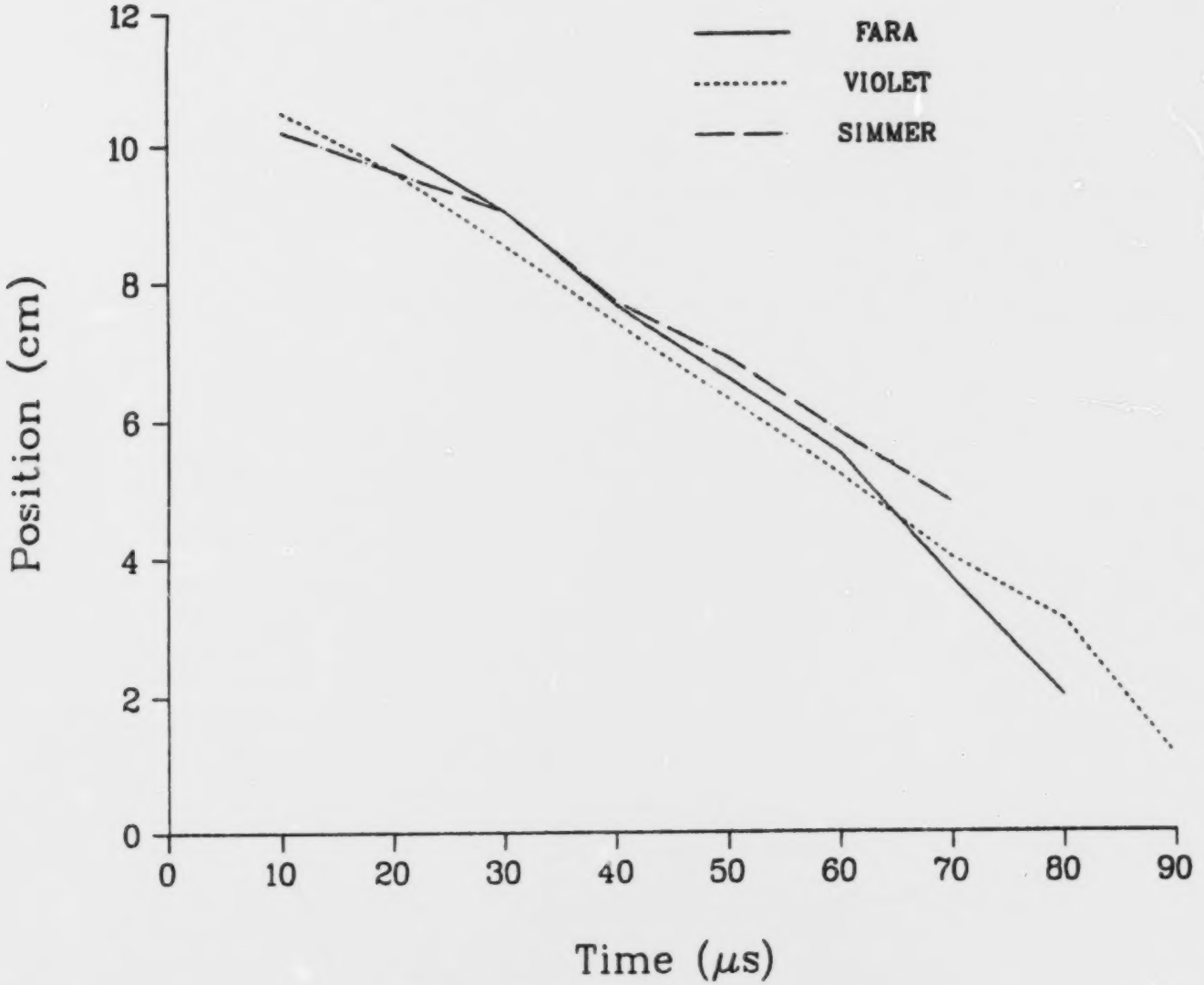

Figure 15 Position of Peak Density for Temperature Spike

BEST DOCUMENT AVAILABLE

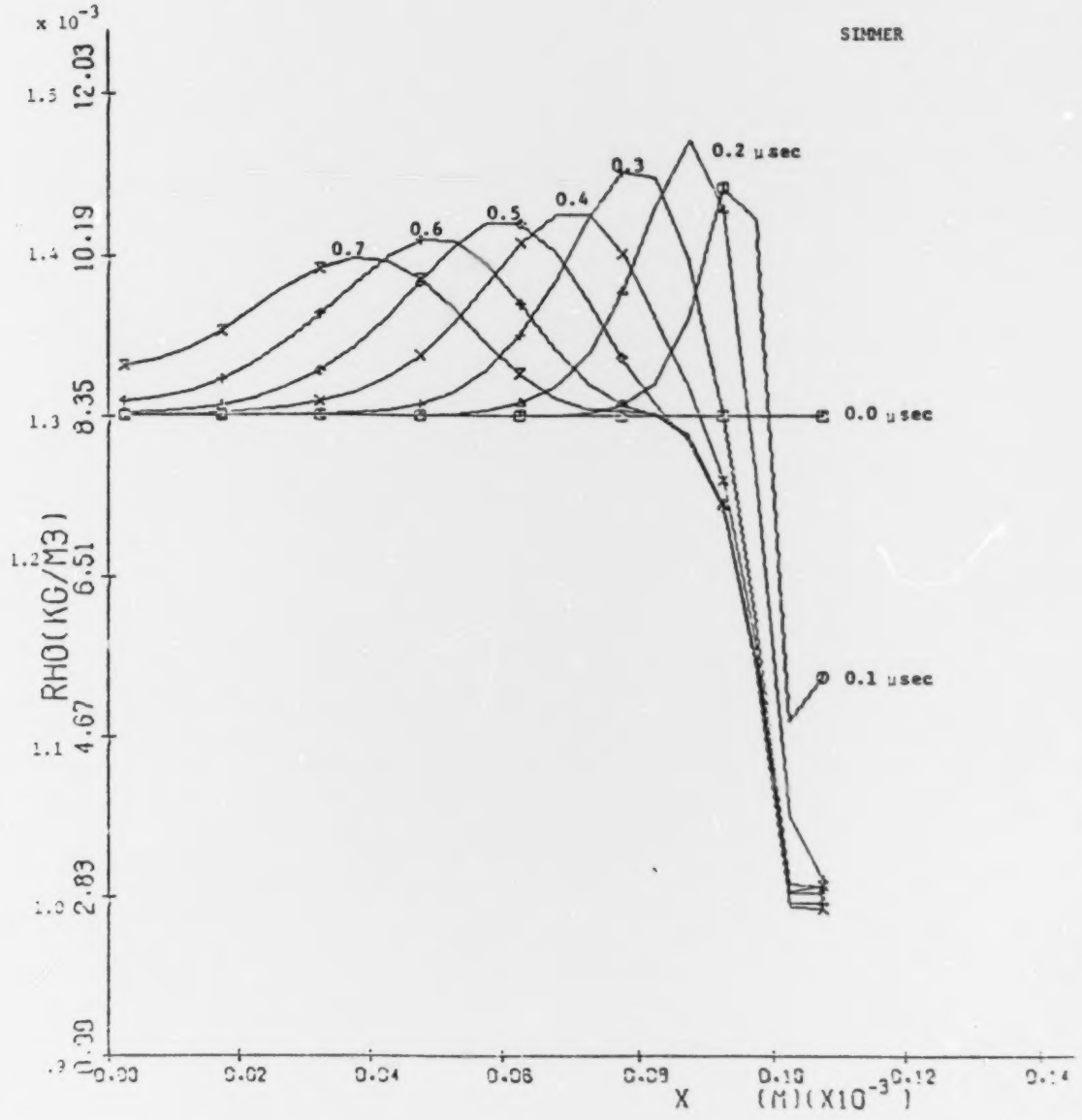

Figure 16 Spreading of Density Pulse in SIMMER Calculation

BEST DOCUMENT AVAILABLE

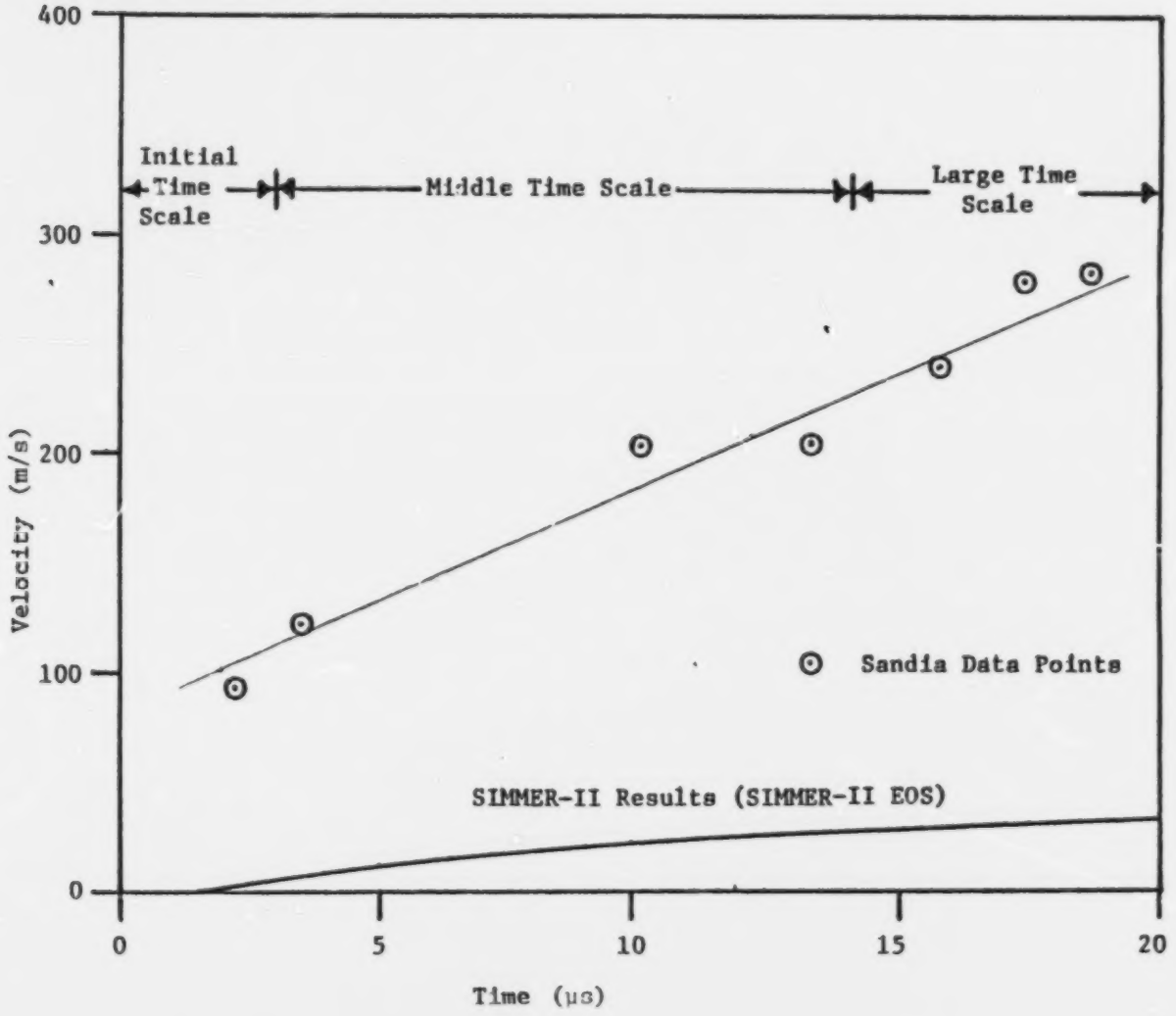

Figure 17 SIMMER-II Velocity Results for 2030 J/g Energy Deposition

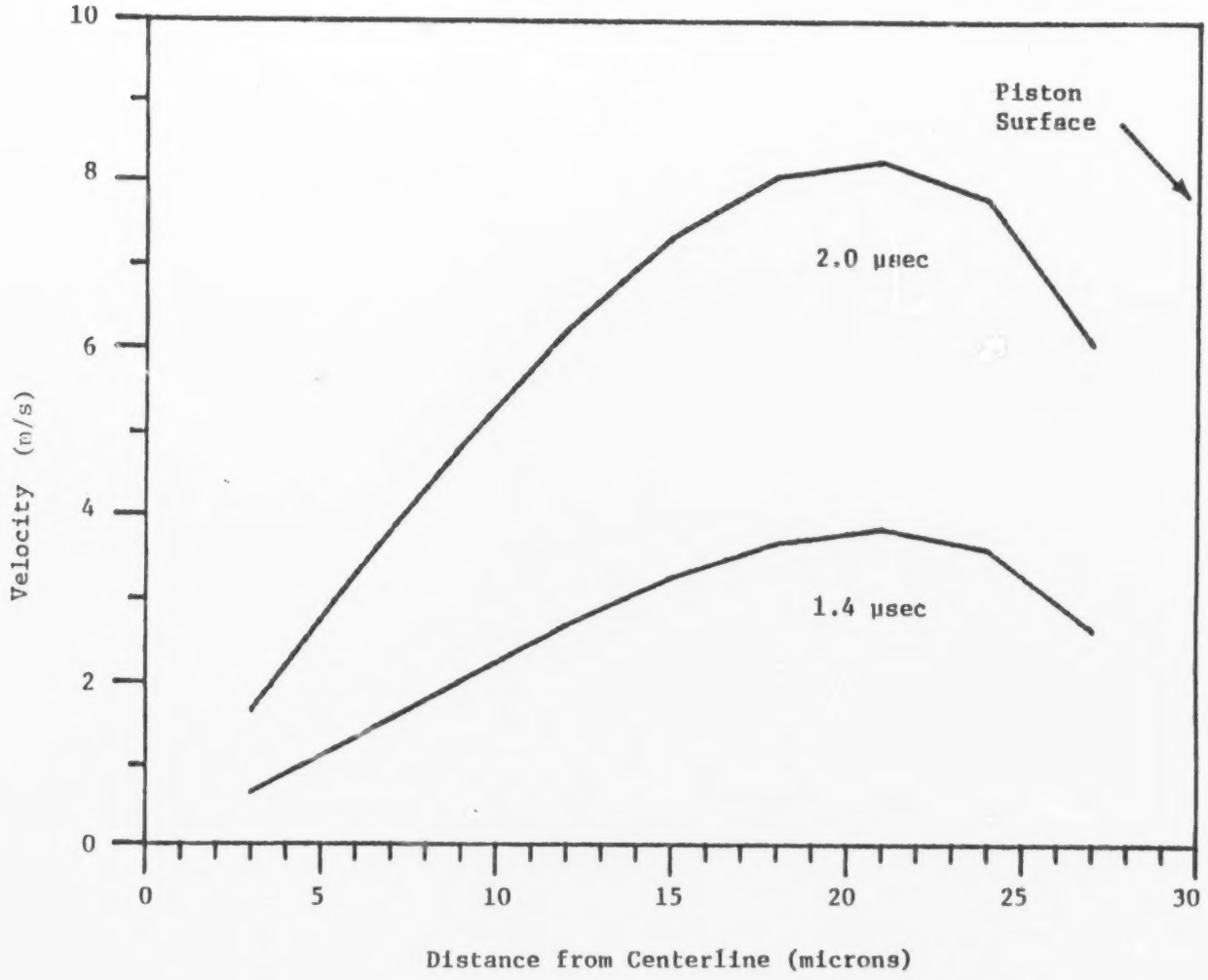

Figure 18 Spatial Liquid Velocity Variation

BEST DOCUMENT AVAILABLE

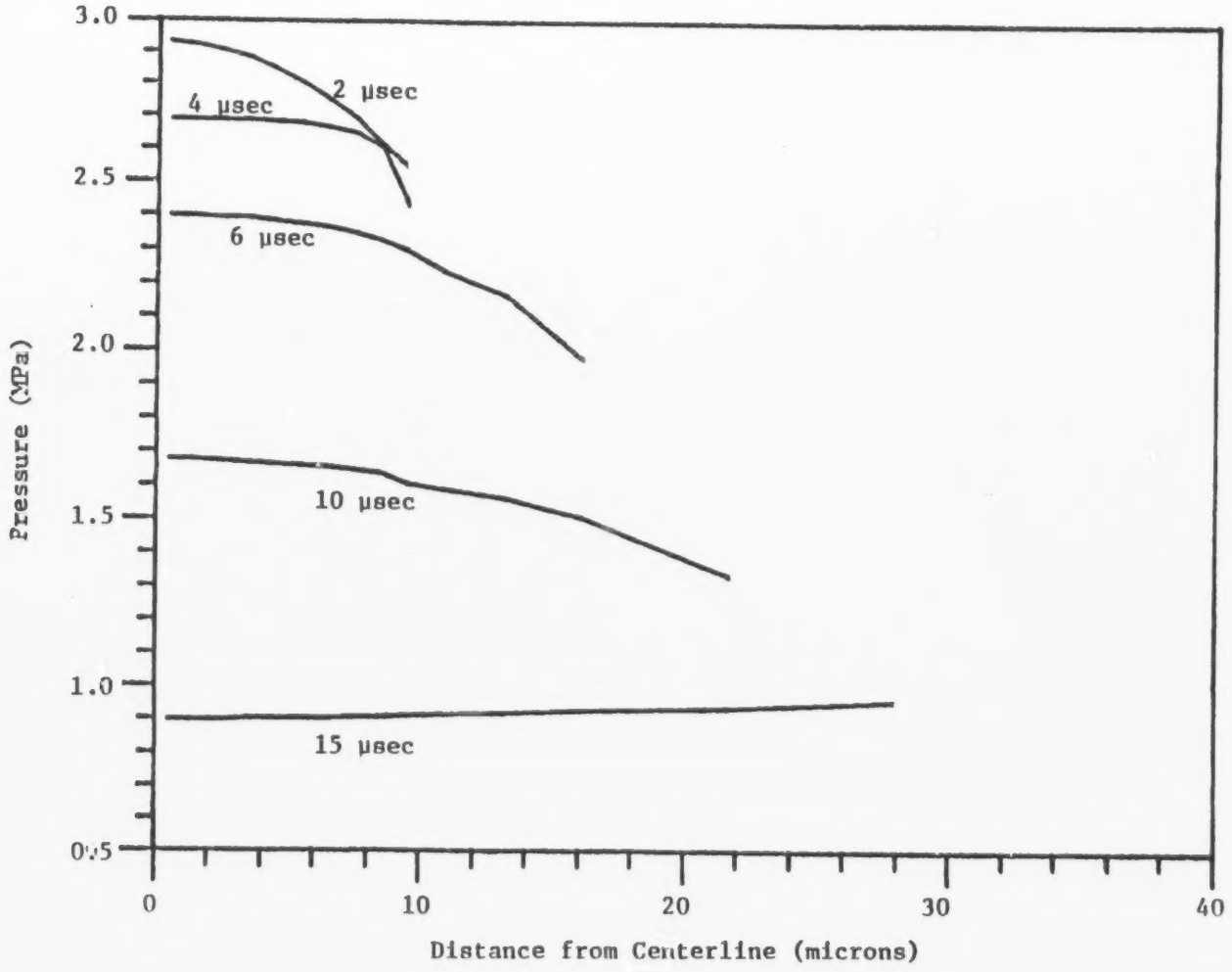

Figure 19 Spatial Variation of the Pressure

BEST DOCUMENT AVAILABLE

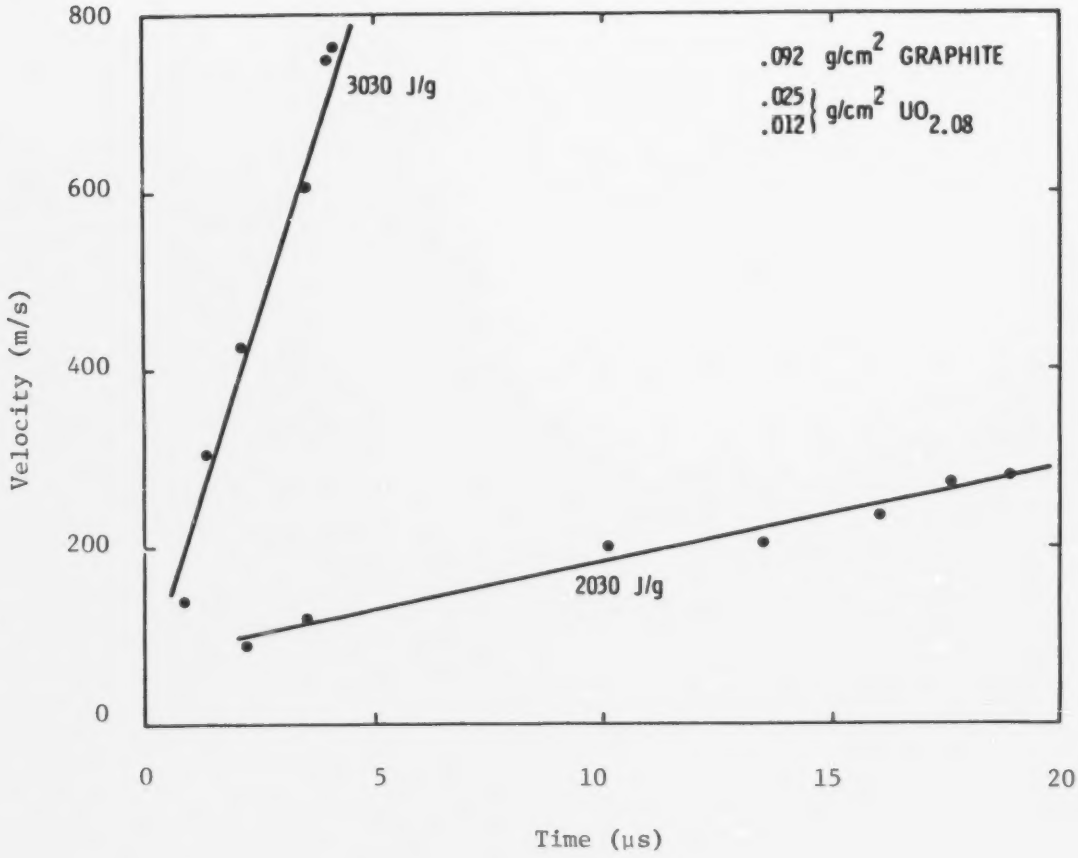

Figure 20 Experimental Data Points for Several Cases

BEST DOCUMENT AVAILABLE

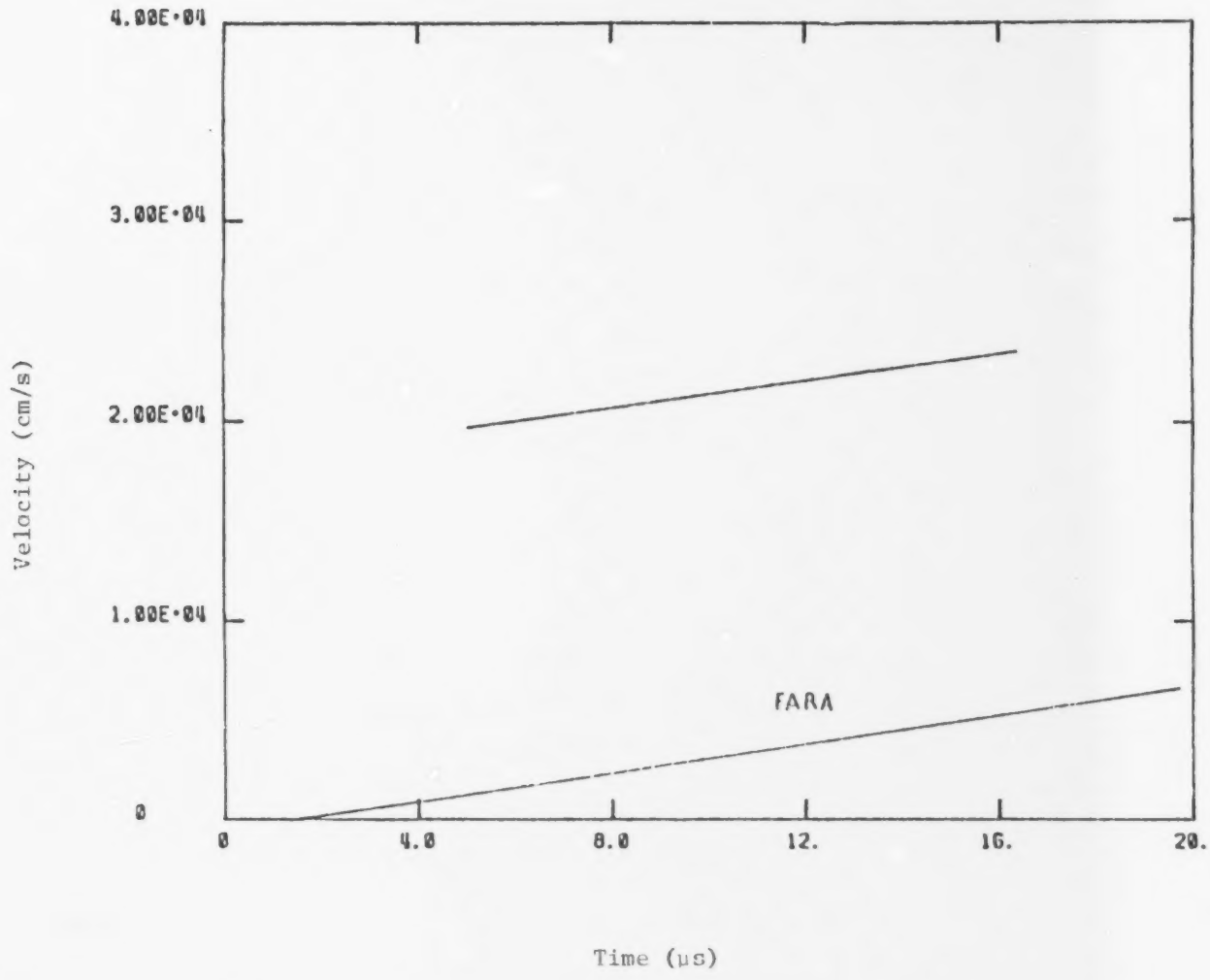

Figure 21 Comparison of Experimental Fit to Numerical Results for the 1860 J/g Energy Pulse

BEST DOCUMENT AVAILABLE

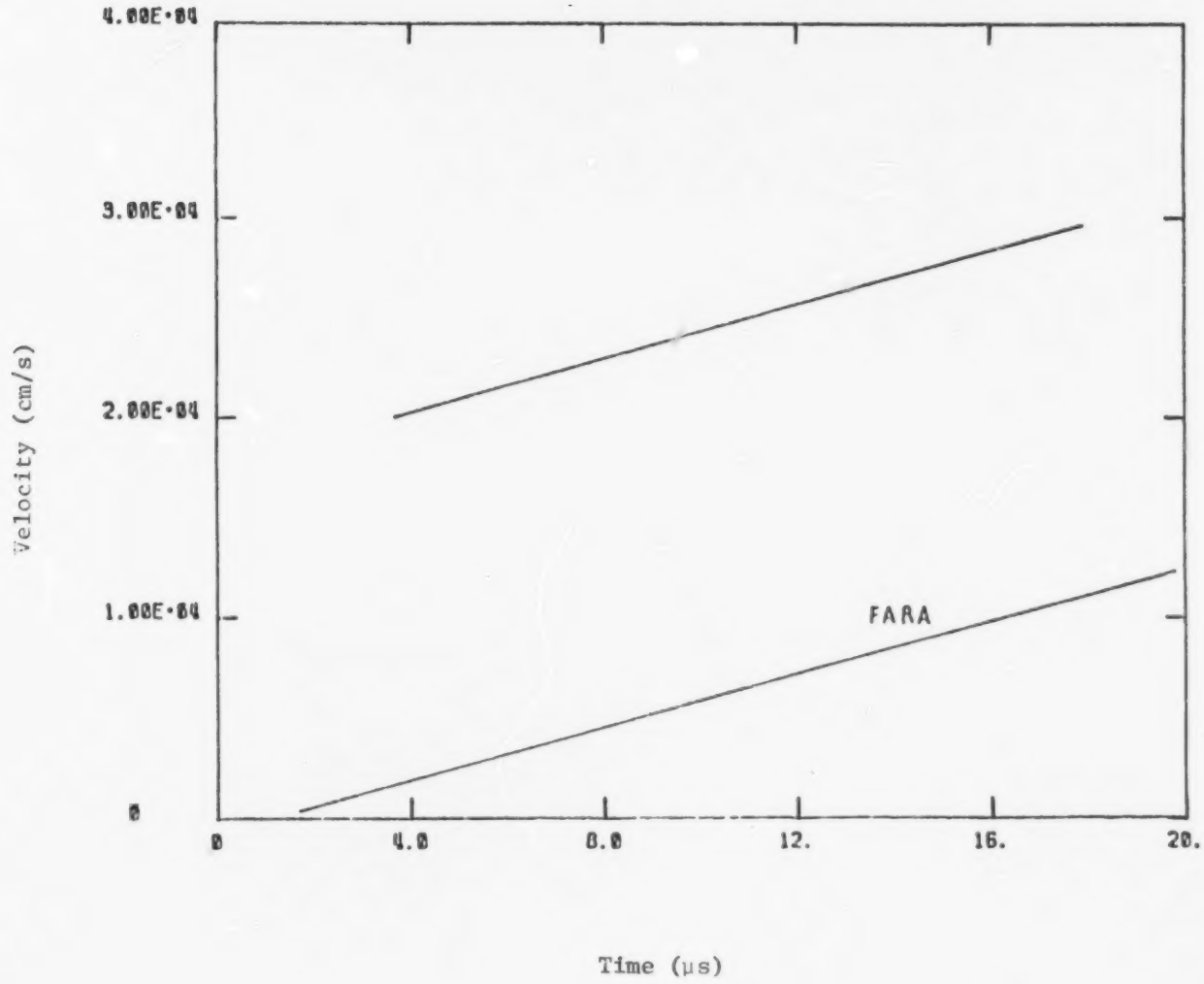

Figure 22 Comparison of Experimental Fit to Numerical Results for the 1990 J/g Energy Pulse

BEST DOCUMENT AVAILABLE

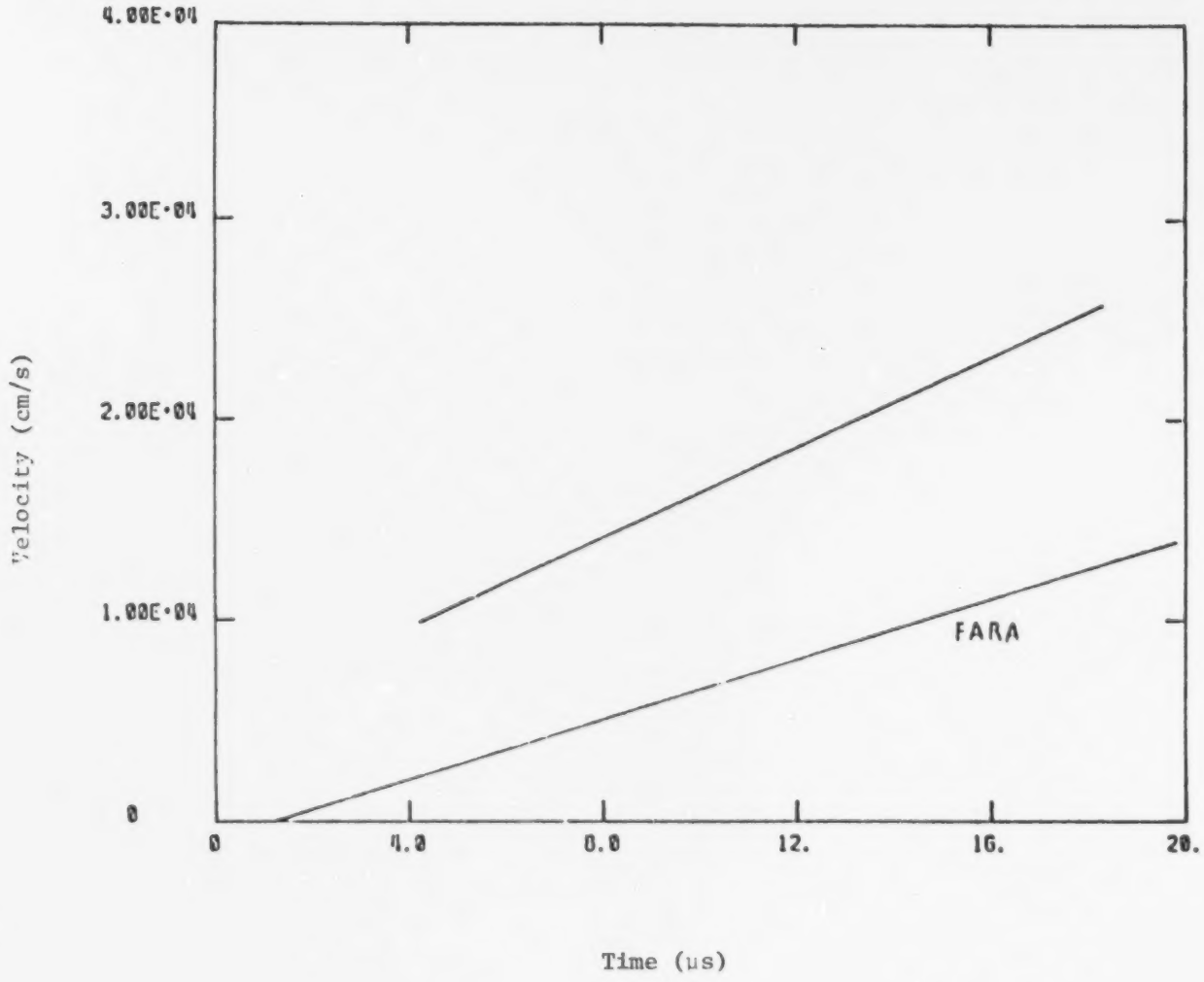

Figure 23 Comparison of Experimental Fit to Numerical Results for the 2030 J/g Energy Pulse

BEST DOCUMENT AVAILABLE

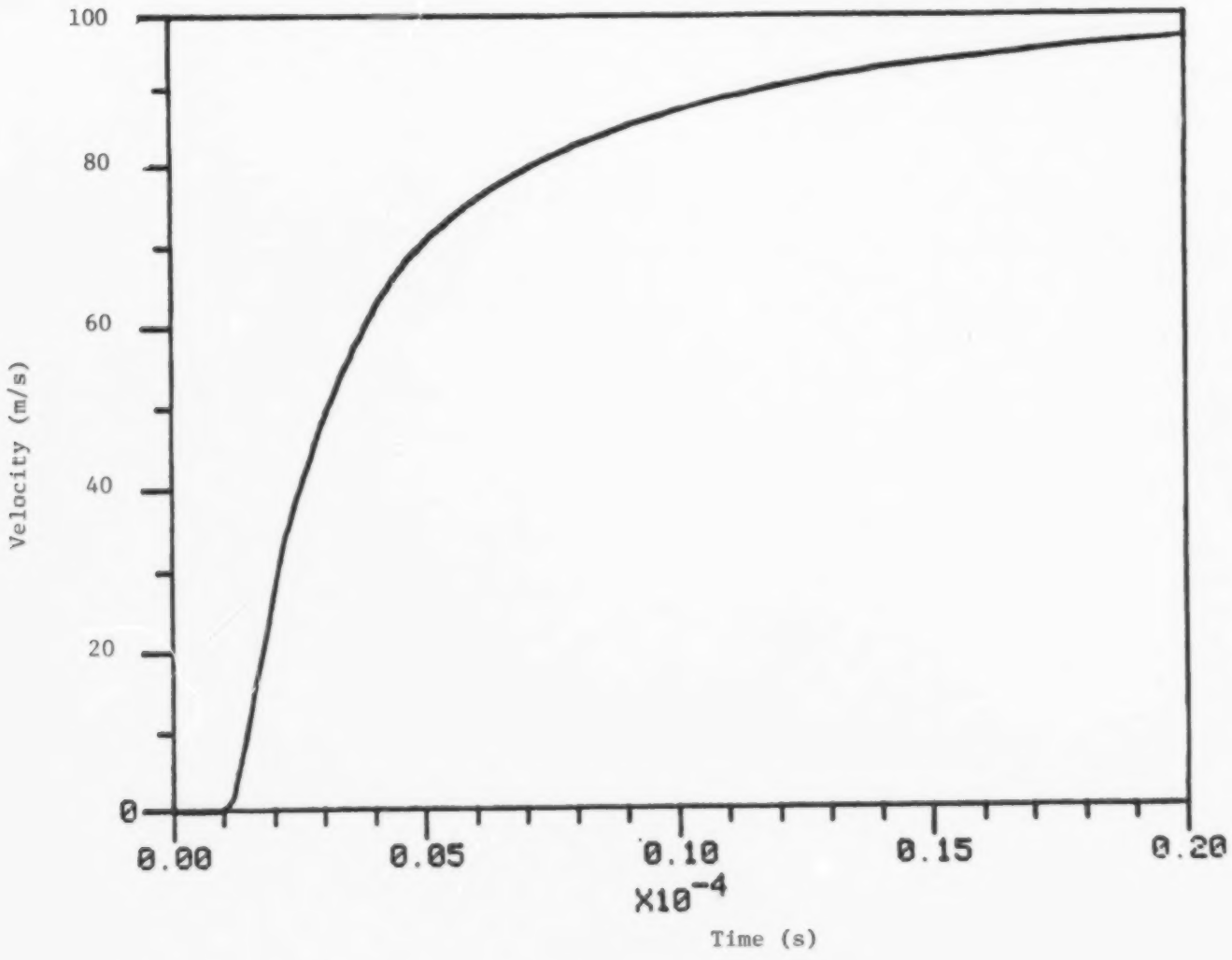

Figure 24 Piston Velocity for 2030 J/g Energy Deposition with Benson EOS

BEST DOCUMENT AVAILABLE

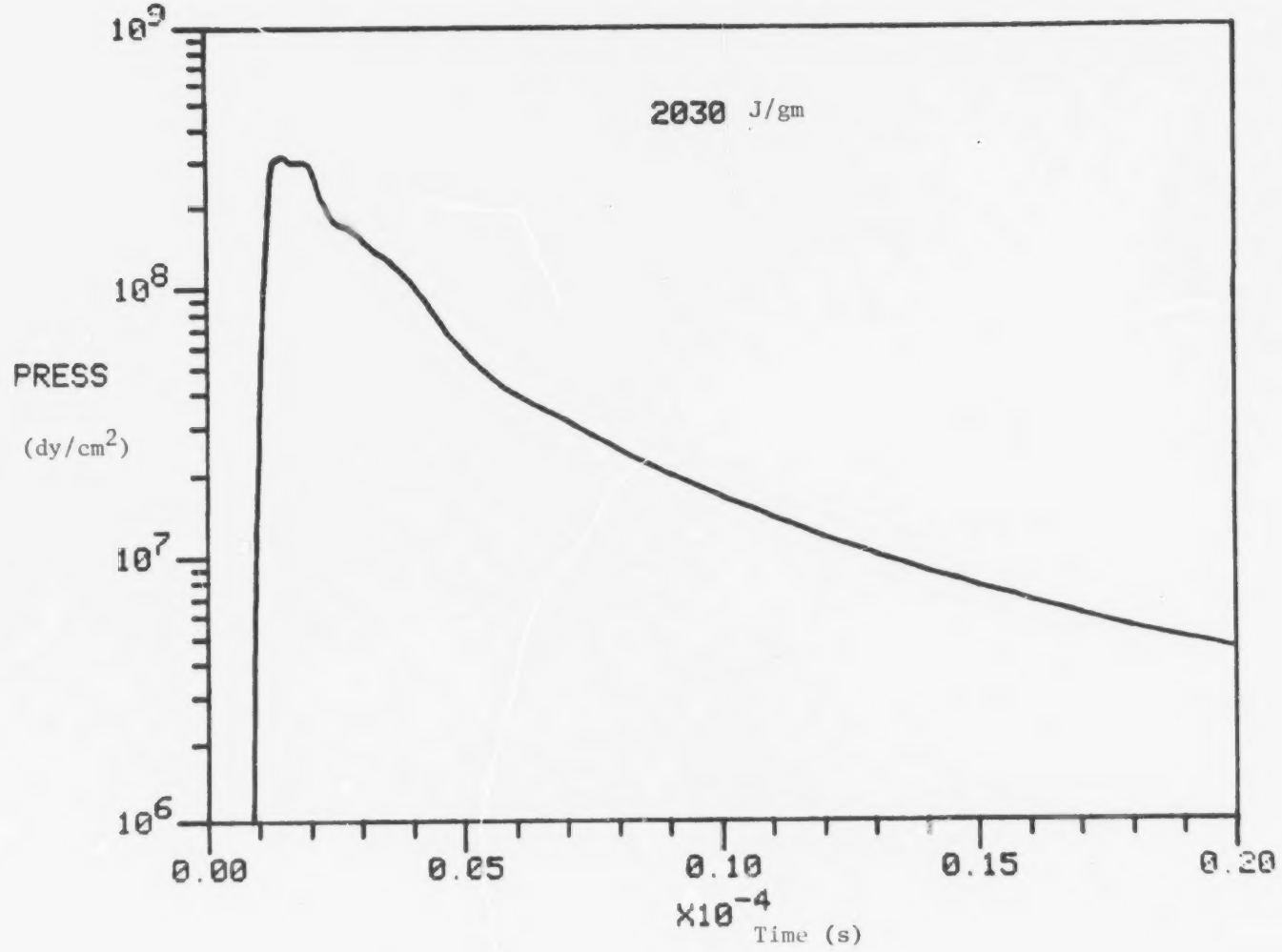

Figure 25 Pressure on Piston Face for 2030 J/g Energy Deposition with Benson EOS

50 BEST DOCUMENT AVAILABLE

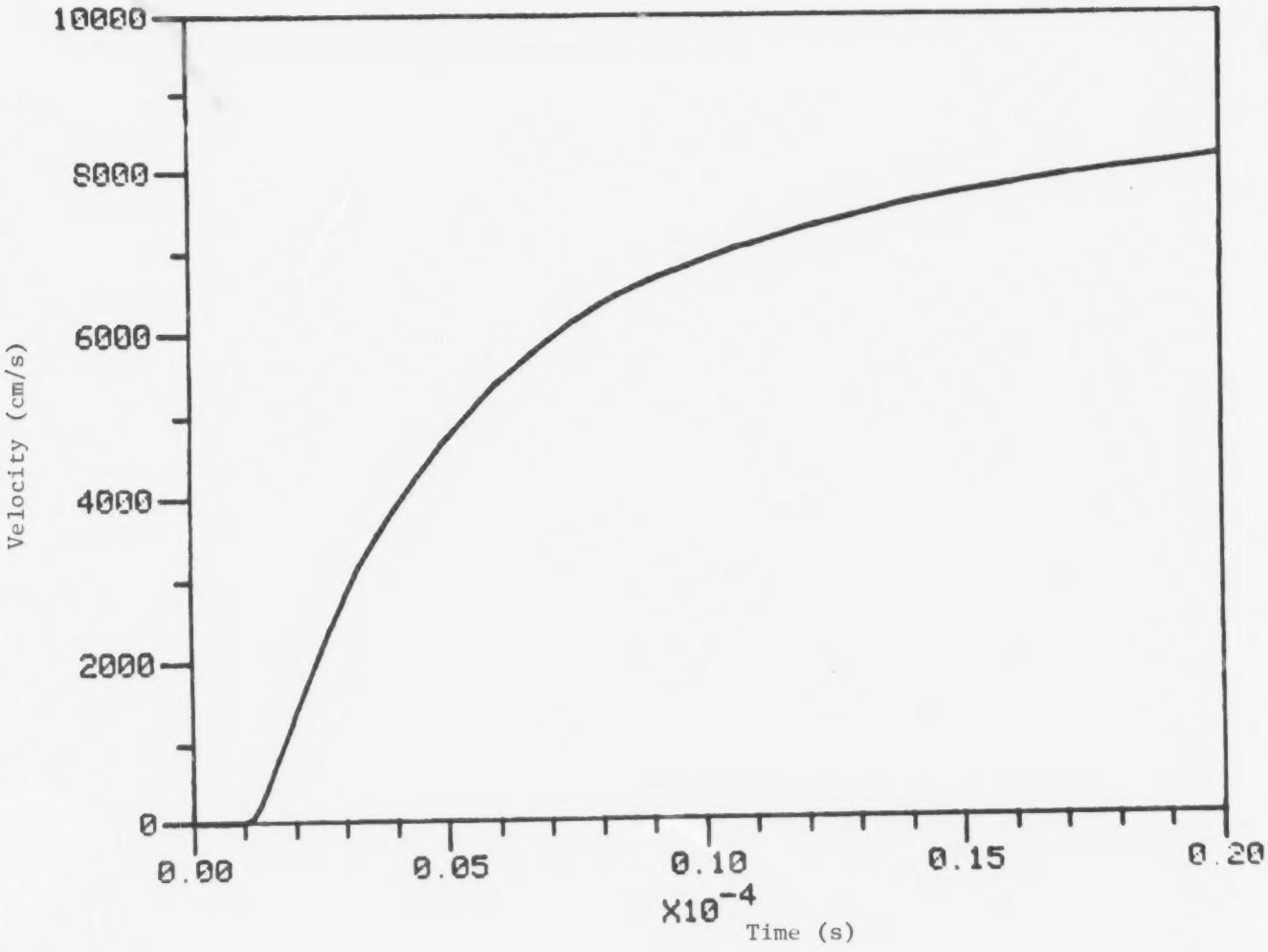

Figure 26 Piston Velocity for 2030 J/g Energy Deposition with Menzes EOS

BEST DOCUMENT AVAILABLE

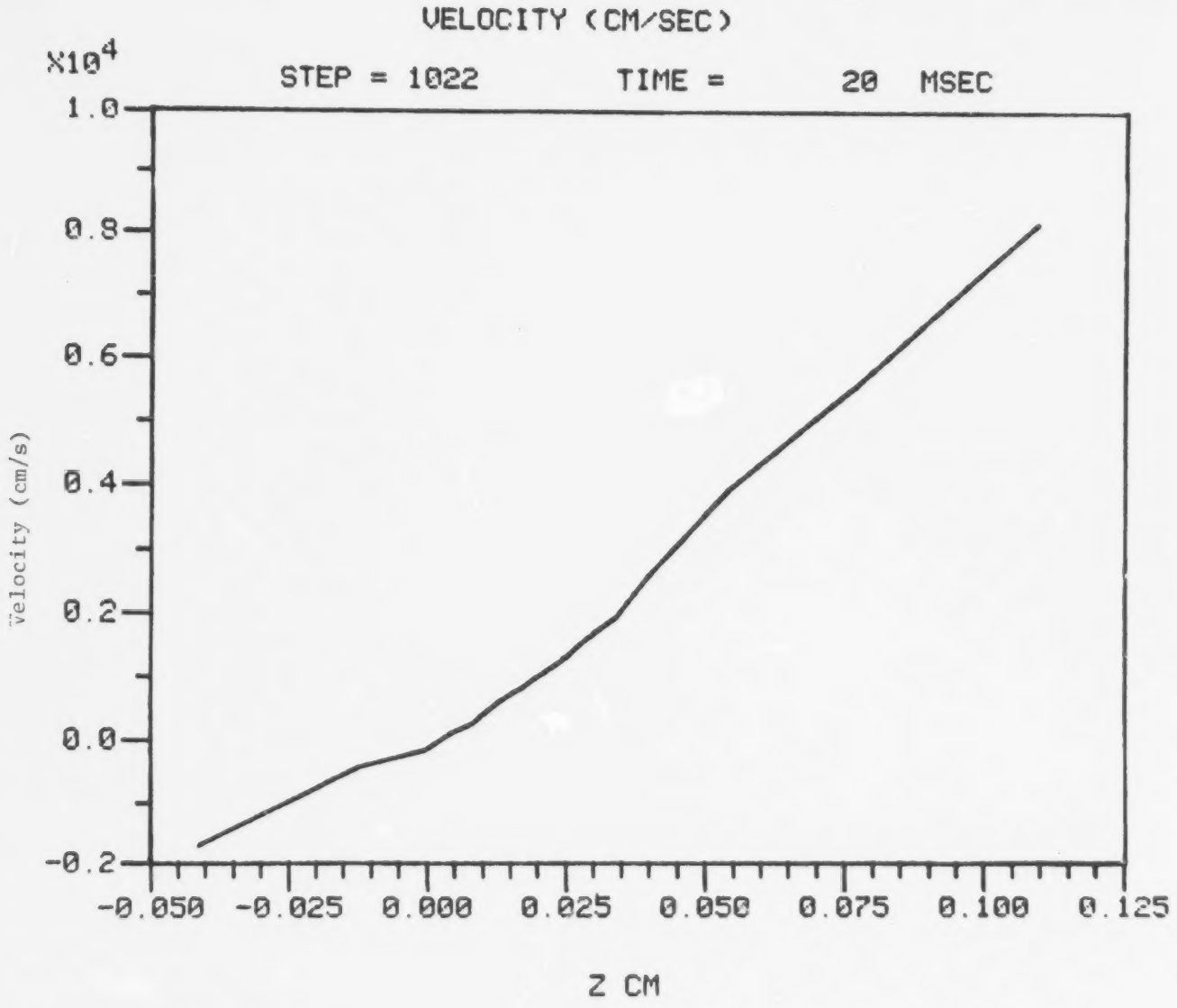

Figure 27 Velocity Profile for 2030 J/g Energy Deposition with Benson EOS

BEST DOCUMENT AVAILABLE

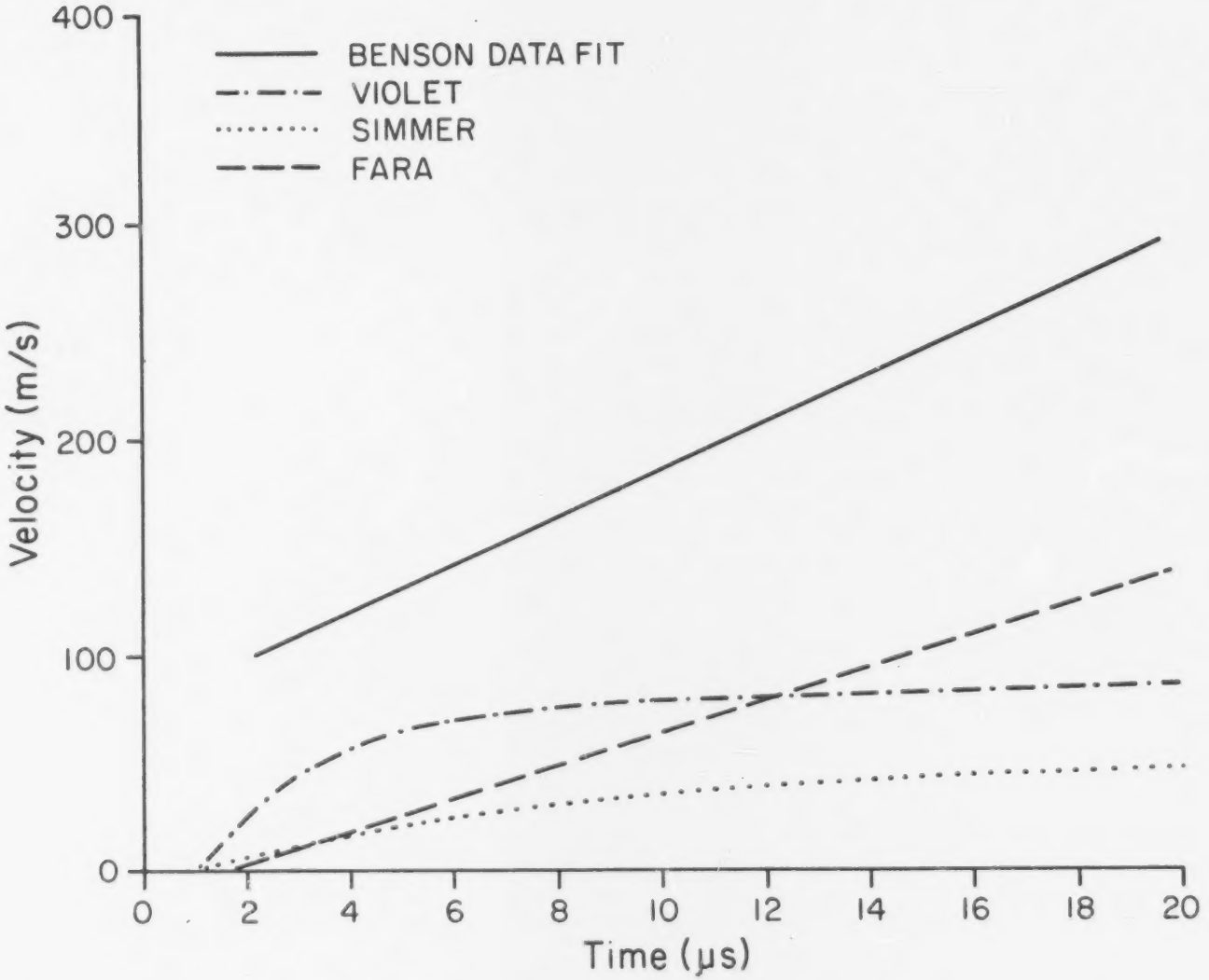

Figure 28 Comparison of the Velocity for 2 030 J/g Deposition.

BEST DOCUMENT AVAILABLE

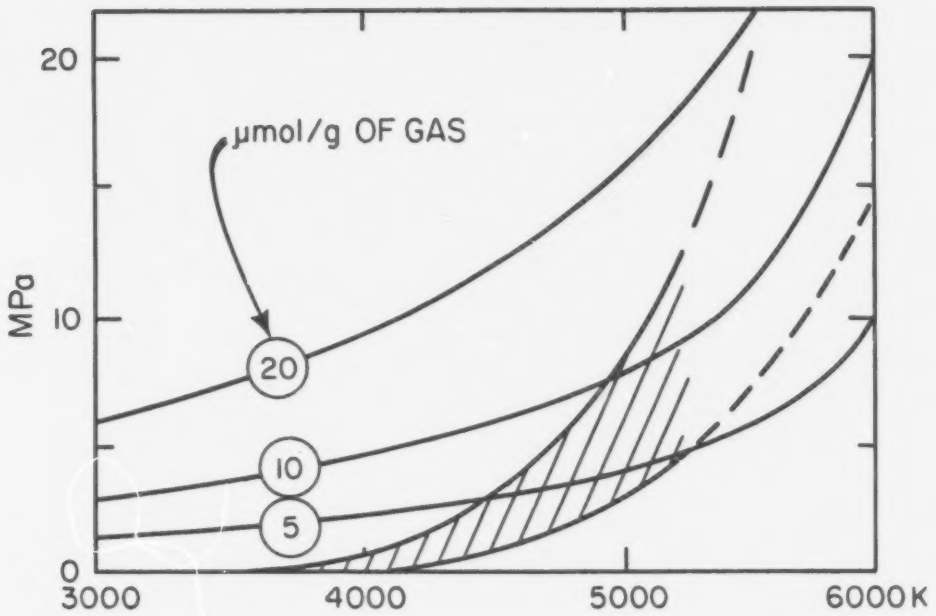

Figure 29 Pressure Contributions from Fuel Impurity Gases Compared to that of Pure Fuel [25].

BEST DOCUMENT AVAILABLE

6. REFERENCES

1. Menzies, C., UKAEA-report TRG-1119 (D) (1966).

2. Ohse, R. W., et al., Proc. of 10th Materials Research Sympo ium on High Temperature Vapors and Gases, Garthersburg, MD (1978).

3. Bober, M., et al., Bericht KFK 2366 (1976).

4. Shanar, J. W., et al., Proc. Europ. Conf. on Thermophys. Prop of Solids at High Temp., Moscow (1976).

5. Reil, K. O. and A. W. Cronenberg, Tran. Am. Nucl. Soc., 27, 576 (1977).

6. Bensen, D. A., Sandia Laboratory Report - SAND-77-0429.

7. Bergeron, E. D., Sandia Laboratory Report - SAND-78-1745.

8. Kerrish, J. and D. Clifton, Nucl. Tech. 16, 531 (1972).

9. Leibowitz, L., et al., Jour. Nucl. Mat. 39 115 (1971).

10. Smith, L. L., LA-7515-M (1980).

11. Smith, L. L., LASL report to be published (1980).

12. Reference deleted. See footnote on page 2.

13. Halbleib, J. A. and W. H. Vandevender, Sandia Laboratory Report SAND-74-0030 (1975).

14. Young, R. A., Engineering Experiment Station, College of Engineering Report, University of Arizona, April (1979).

15. MacInnes, D. A., Proc. Symp. Thermodynamics of Nuclear Materials, Julich, UKAEA Report SRD R151, (1979).

16. Zivi, S. M., et al., Nucl. Sci. Eng., 56, 229 (1975).

17. Reil, K. O., M. F. Young and T. R. Schmidt, Sandia Laboratory Report SAND-79-1561 (1978).

18. Booth, D. L., UKAEA Report TRG 1759 (1968).

19. Harlow, F. H. and A. A. Amsden, Jour. of Comp. Phys., V 8, No. 2, 197 (1971).

20. Nakmura, S., Computational Methods in Engineering Science, Wiley and Sons (1977).

21. Ganapol, B. D., in preparation ANL (1977).

22. Harlow, F. and A. Amsden, LA-4700 June (1971).

23. Benson, D. A. J. Appl. Phys., 47, 4873 (1973).

24. Fink, J. K., M. G. Chasanov and L. Liebowitz, ANL-CEN-RSD-77-1 ANL (1977).

25. Breitung, W. M., Sandia Laboratory Report, SAND-80-1277 (NUREG/CR-1510) (1980), "Contamination Control in Sandia Equation-of-State Experiments."

26. McTaggert, M. H. and J. R. Findley, ANRE-44-96-4.

27. Wright, S. A. et al., Tran. Am. Nucl. Soc., 38, 372 (1981).

NRC FORM 335 (11.81) U.S. NUCLEAR REGULATORY COMMISSION

BIBLIOGRAPHIC DATA SHEET

1. REPORT NUMBER *(Assigned by DDC)*: NUREG/CR-2520

4. TITLE AND SUBTITLE *(Add Volume No., if appropriate)*: A Hydrodynamic Analysis of the Electron Beam Vaporization Experiments for UO_2

2. *(Leave blank)*

3. RECIPIENT'S ACCESSION NO.

7. AUTHOR(S): B. D. Ganapol, B. A. Clark, M. S. Smith, G. W. Sowers

5. DATE REPORT COMPLETED: MONTH June YEAR 1982

9. PERFORMING ORGANIZATION NAME AND MAILING ADDRESS *(Include Zip Code)*:
Department of Nuclear and Energy Engineering
The University of Arizona
Tucson, Arizona 85721

DATE REPORT ISSUED: MONTH July YEAR 1982

6. *(Leave blank)*

8. *(Leave blank)*

12. SPONSORING ORGANIZATION NAME AND MAILING ADDRESS *(Include Zip Code)*:
Division of Accident Evaluation
Office of Nuclear Regulatory Research
U.S. Nuclear Regulatory Commission
Washington, D.C. 20555

10. PROJECT TASK/WORK UNIT NO.

11. FIN NO.: A4065

13. TYPE OF REPORT: Technical

PERIOD COVERED *(Inclusive dates)*: 10/1/79 - 9/31/81

15. SUPPLEMENTARY NOTES

14. *(Leave blank)*

16. ABSTRACT *(200 words or less)*

The electron-beam experiments designed to generate high temperature vapor pressure data for UO_2 vapor is analyzed by three hydrodynamic codes SIMMER, FARA, and VIOLET. The physical and numerical modeling in each code is different thus providing a modeling error associated with the analysis. Agreement with the experiment is rather poor indicating that the rate dependent specific heat capacity model proposed by Benson may not be a physical reality.

17. KEY WORDS AND DOCUMENT ANALYSIS

17a. DESCRIPTORS

UO_2 Vapor
Equation of State UO_2

17b. IDENTIFIERS/OPEN-ENDED TERMS

18. AVAILABILITY STATEMENT: Unlimited

19. SECURITY CLASS *(This report)*: Unclassified

21. NO. OF PAGES

20. SECURITY CLASS *(This page)*: Unclassified

22. PRICE

NRC FORM 335 (11-81)

57 BEST DOCUMENT AVAILABLE